Resource

Cell

A Suite of Transgenic Driver and Reporter Mouse Lines with Enhanced Brain-Cell-Type Targeting and Functionality

Graphical Abstract

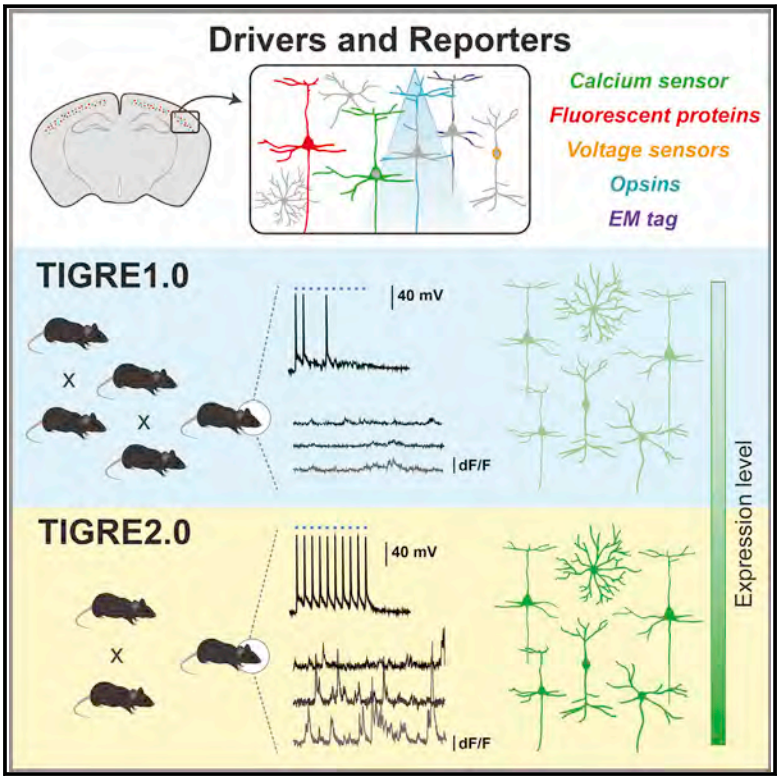

Highlights

- 23 new driver lines and 26 new reporter lines for a wide range of applications
- TIGRE2.0 reporters have viral-like transgene expression level in diverse cell types
- New calcium- or voltage-sensing reporters with the former functionally characterized
- Comparative analysis of new optogenetic effectors with complementary properties

Authors

Tanya L. Daigle, Linda Madisen, Travis A. Hage, ..., Lu Li, Bosiljka Tasic, Hongkui Zeng

Correspondence

hongkuiz@alleninstitute.org

In Brief

An expanded toolkit of transgenic mouse lines for exploring the organization, function, and development of mammalian neural circuits.

Daigle et al., 2018, Cell *174*, 465–480
July 12, 2018
https://doi.org/10.1016/j.cell.2018.06.035

CellPress

Resource

Cell

A Suite of Transgenic Driver and Reporter Mouse Lines with Enhanced Brain-Cell-Type Targeting and Functionality

Tanya L. Daigle,[1,4] Linda Madisen,[1,4] Travis A. Hage,[1] Matthew T. Valley,[1] Ulf Knoblich,[1] Rylan S. Larsen,[1] Marc M. Takeno,[1] Lawrence Huang,[1] Hong Gu,[1] Rachael Larsen,[1] Maya Mills,[1] Alice Bosma-Moody,[1] La' Akea Siverts,[1] Miranda Walker,[1] Lucas T. Graybuck,[1] Zizhen Yao,[1] Olivia Fong,[1] Thuc Nghi Nguyen,[1] Emma Garren,[1] Garreck H. Lenz,[1] Mariya Chavarha,[2] Julie Pendergraft,[1] James Harrington,[1] Karla E. Hirokawa,[1] Julie A. Harris,[1] Philip R. Nicovich,[1] Medea J. McGraw,[1] Douglas R. Ollerenshaw,[1] Kimberly A. Smith,[1] Christopher A. Baker,[1] Jonathan T. Ting,[1] Susan M. Sunkin,[1] Jérôme Lecoq,[1] Michael Z. Lin,[2] Edward S. Boyden,[3] Gabe J. Murphy,[1] Nuno M. da Costa,[1] Jack Waters,[1] Lu Li,[1] Bosiljka Tasic,[1] and Hongkui Zeng[1,5,*]

[1]Allen Institute for Brain Science, Seattle, WA 98109, USA

[2]Departments of Neurobiology and Bioengineering, Stanford University School of Medicine, Stanford, CA 94305, USA

[3]MIT Media Lab and McGovern Institute, Departments of Biological Engineering and Brain and Cognitive Sciences, Massachusetts Institute of Technology, Cambridge, MA 02139, USA

[4]These authors contributed equally

[5]Lead Contact

*Correspondence: hongkuiz@alleninstitute.org

https://doi.org/10.1016/j.cell.2018.06.035

SUMMARY

Modern genetic approaches are powerful in providing access to diverse cell types in the brain and facilitating the study of their function. Here, we report a large set of driver and reporter transgenic mouse lines, including 23 new driver lines targeting a variety of cortical and subcortical cell populations and 26 new reporter lines expressing an array of molecular tools. In particular, we describe the TIGRE2.0 transgenic platform and introduce Cre-dependent reporter lines that enable optical physiology, optogenetics, and sparse labeling of genetically defined cell populations. TIGRE2.0 reporters broke the barrier in transgene expression level of single-copy targeted-insertion transgenesis in a wide range of neuronal types, along with additional advantage of a simplified breeding strategy compared to our first-generation TIGRE lines. These novel transgenic lines greatly expand the repertoire of high-precision genetic tools available to effectively identify, monitor, and manipulate distinct cell types in the mouse brain.

INTRODUCTION

The nervous system is composed of myriad cell types in a highly organized and coordinated manner to produce function (Zeng and Sanes, 2017). Neuronal cell types have diverse molecular, morphological, and physiological properties and are interconnected to form multiple levels of neural circuits that generate behavior. Efforts have been underway to systematically profile these properties at the single-cell level and develop cell-type classification schemes; to build connectomes at micro-, meso-, and macroscopic levels; and to probe neuronal activities in behaving animals. All these levels of investigation are necessary to obtain fundamental understanding of how the nervous system works. And central to all these investigations is our ability to gain access to individual cell types, to perform circuit dissection, and to connect information gathered at gene, cell, and network levels (Huang and Zeng, 2013; Luo et al., 2008).

Cell-type-specific genetic tools constitute a powerful approach for the study of brain function via targeted expression of a variety of molecular sensors and probes in different cell types. In the mouse, the Cre/Lox system has been widely applied with a large number of Cre driver transgenic mouse lines now available. This, combined with other recombinases and transcriptional regulation systems (Dymecki et al., 2010; Huang and Zeng, 2013; Madisen et al., 2015), has allowed more refined and flexible control of specific cell populations. Recent advances in single-cell transcriptomics have yielded novel cell-type-specific marker genes, and this, coupled with the development of new and better genetically encoded molecular sensors and probes, continues to fuel the genetic-tool-generation pipeline. Overall, the creation of new cell-type-specific genetic tools holds tremendous promise in enabling better labeling, monitoring, and manipulation of these neural circuit components and, ultimately, detailed mechanistic insight on brain function. At the same time, the demand for genetic tools with better specificity and performance still far exceeds their current availability, and much work is needed to convert promise into reality.

For expressing genetic tools, in addition to the commonly used Rosa26 locus, we previously explored another permissive genomic locus, TIGRE, to establish a series of intersectional reporter lines controlled by Cre and a tetracycline-regulated transcriptional transactivator, tTA (Madisen et al., 2015; Zeng et al., 2008). We found that these TIGRE-based lines afforded substantially higher reporter and effector gene expression compared to the Rosa26-based lines, likely due to

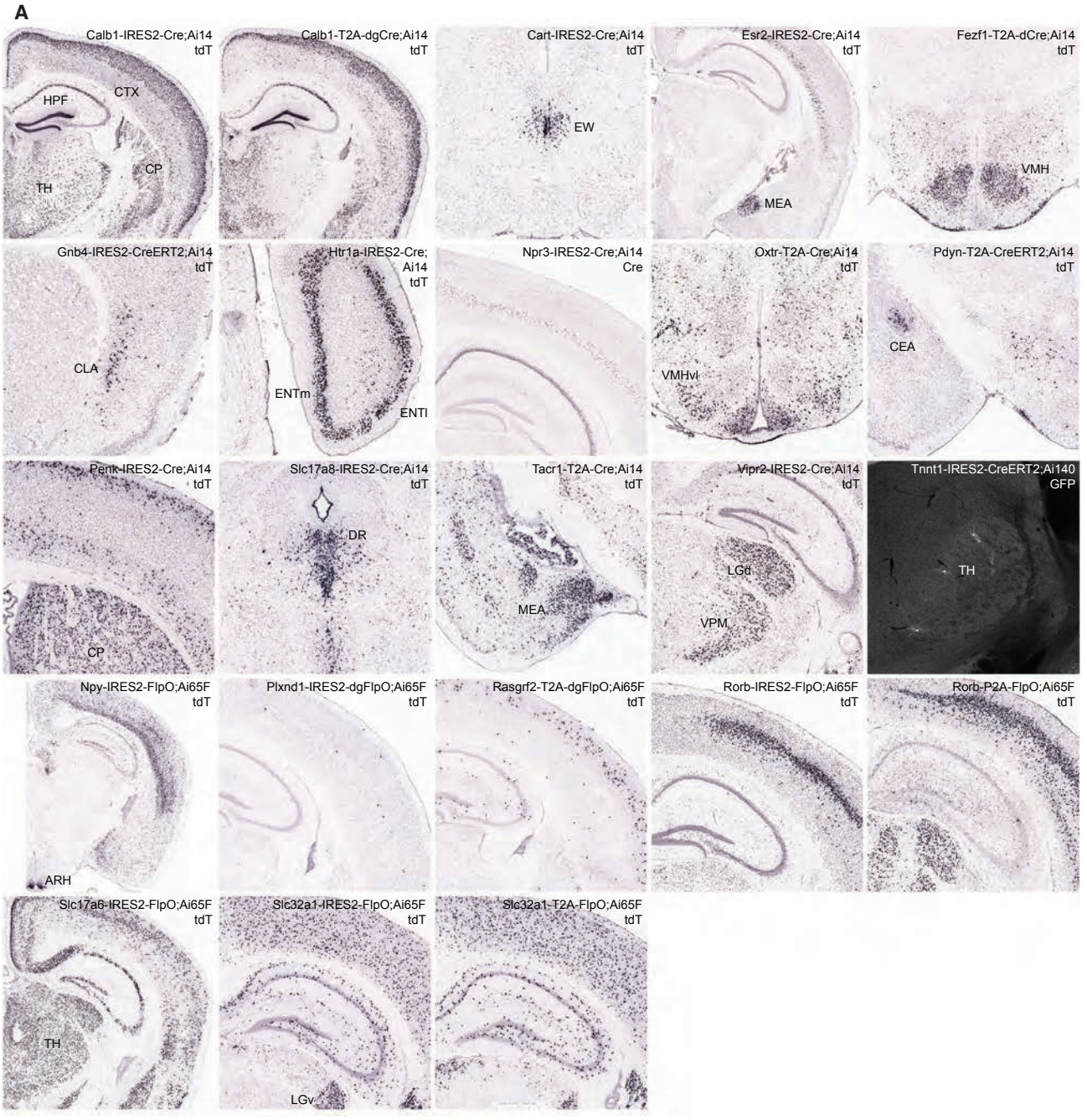

(legend on next page)

tTA/TRE-mediated transcriptional amplification. This is a critical improvement as sufficiently high-level expression of many molecular tools, such as fluorescent proteins, calcium indicators, and channelrhodopsins, is needed to allow full-extent visualization of fine neuronal structures and effective reporting or manipulation of neuronal activities *in vivo* in a minimally invasive fashion.

In this paper, we report a large and diverse set of new cell-type-specific transgenic mouse lines, including 23 new driver lines (15 Cre and 8 Flp lines) and 26 new reporter lines. The reporter lines express a variety of molecular tools that will enable a wide range of applications. In particular, we have developed a new transgene design in the TIGRE locus, in which a Cre-dependent tTA-expressing transgene cassette was co-integrated into TIGRE along with the Cre and tTA-dependent reporter gene cassette. This approach converts the TIGRE reporter lines into simple Cre-reporters while retaining the tTA-mediated transcriptional amplification. We name these second-generation TIGRE lines TIGRE2.0 and our previous Cre- and tTA-dependent TIGRE lines TIGRE1.0. TIGRE2.0 lines simplify breeding strategies and expand the repertoire of cell types with strong reporter gene expression to nearly all the cell types we have examined. Single-cell transcriptomics analysis shows that TIGRE2.0 reporters have reached a transgene expression level comparable to that of strong promoter-driven recombinant adeno-associated virus (AAV) vectors, breaking a significant barrier in single-copy targeted-insertion transgenesis. Importantly, we demonstrate superior functionality of many new transgenic lines and also disclose side effects observed in animals with extremely high-level and widespread transgene expression in some circumstances. Experiences gained and lessons learned in the extensive study reported here will be invaluable for the utilization and further development of optimal genetic targeting strategies.

RESULTS

The transgenic mouse program at the Allen Institute for Brain Science has generated transgenic mouse lines for cell-type-specific labeling and manipulation for the past 10 years (Harris et al., 2014; Madisen et al., 2010, 2012, 2015). A total of 56 driver lines and 54 reporter lines have been generated. Transgene expression patterns in the entire mouse brain for the majority of these lines have been systematically characterized using our RNA *in situ* hybridization (ISH) pipeline, and all the data are available at the brain-map.org portal (http://connectivity.brain-map.org/transgenic; http://www.alleninstitute.org/what-we-do/brain-science/research/products-tools/). To provide a comprehensive and centralized overview, all transgenic lines generated in the Allen Institute are summarized in Table S1 for driver lines and Table S2 for reporter lines. Most of these lines have been deposited to the Jackson Laboratory, and they have been widely utilized in the broad research community. Out of these 110 lines, 33 driver and 28 reporter lines have been described in previous publications, whereas the remaining 23 driver and 26 reporter lines are formally reported for the first time in this paper.

New Cre and Flp Driver Lines Targeting a Variety of Cell Populations

The 23 new driver lines (Table S1) were created by inserting Cre or FlpO into the C terminus of an endogenous gene via homologous recombination, using either conventional or CRISPR/Cas9-mediated approaches, with driver gene expression mediated by either an internal ribosome entry site (IRES, variant IRES2 in particular) or a 2A peptide (T2A or P2A) sequence. Out of these, 15 lines express variants of Cre, including Cre itself, tamoxifen-inducible CreERT2, trimethoprim (TMP)-inducible dCre (DHFR-Cre) or dgCre (DHFR-GFP-Cre) (Sando et al., 2013), and 8 lines express FlpO or its TMP-inducible version dgFlpO (DHFR-GFP-FlpO).

Target genes chosen for making Cre and FlpO driver lines to supplement existing lines include cortical layer-selective genes that label mainly excitatory neurons (e.g., *Calb1*, *Htr1a*, *Npr3*, *Plxnd1*, *Rasgrf2*, and *Rorb*), neuropeptide and receptor genes (e.g., *Cart*, *Esr2*, *Npy*, *Oxtr*, *Pdyn*, *Penk*, *Tacr1*, and *Vipr2*), genes targeting specific cell populations (e.g., *Fezf1* for ventromedial hypothalamus, *Gnb4* for claustrum, and *Tnnt1* for thalamus), and pan-GABAergic (*Slc32a1*, also known as *Vgat*) or glutamatergic (*Slc17a6*, also known as *Vglut2*, and *Slc17a8*, also known as *Vglut3*) genes. Expression patterns of the driver genes and the tdTomato reporter gene were examined by ISH (Figure 1A).

The expression patterns of all driver transgenes largely recapitulate the adult (P56) expression patterns of their endogenous target genes. On the other hand, the expression patterns of Cre and Flp reporters are often more widespread, likely due to the cumulative recombination from transient expression of the driver genes in developmental or adult stages. An observed trend is that IRES-mediated drivers tend to drive more faithful expression of the reporters, whereas 2A-mediated drivers often lead to more widespread reporter expression. Also, dCre and dgCre can mediate efficient recombination as do Cre and FlpO, whereas CreERT2 and dgFlpO tend to have less efficient recombination as indicated by the sparser activation of the reporters.

We examined the co-expression of tdTomato reporter with a pan-GABAergic marker *Gad1* by double fluorescence *in situ* hybridization (dFISH) in several cortical layer-selective driver lines

Figure 1. New Cre and Flp Driver Lines Targeting Specific Cell Populations in the Brain

(A) Selected images from ISH characterization of all new driver lines using either tdTomato reporter probe or Cre probe as indicated on each panel. Full ISH datasets are viewable at http://connectivity.brain-map.org/transgenic. Ai14 was used to examine all Cre lines, and Ai65F was used for all FlpO lines. The only exception is Tnnt1-IRES2-CreERT2, which was crossed to a new TIGRE2.0 reporter Ai140, and TissueCyte imaging shows extremely sparse GFP labeling of thalamic neurons (after 1-day tamoxifen induction at P10). For region acronyms, see STAR Methods.

(B) Examination of excitatory and inhibitory neuronal labeling in example cortical layer-selective driver lines. Representative images of dFISH in VISp, using tdTomato reporter (green) and pan-GABAergic marker *Gad1* (red) probes, are shown. The extent of reporter expression in inhibitory neurons varied from none (Plxnd1-IRES2-dgFlpO, Rorb-P2A-FlpO) to a few cells (Rasgrf2-T2A-dgFlpO) to many cells (Calb1-IRES2-Cre).

See also Tables S1 and S3.

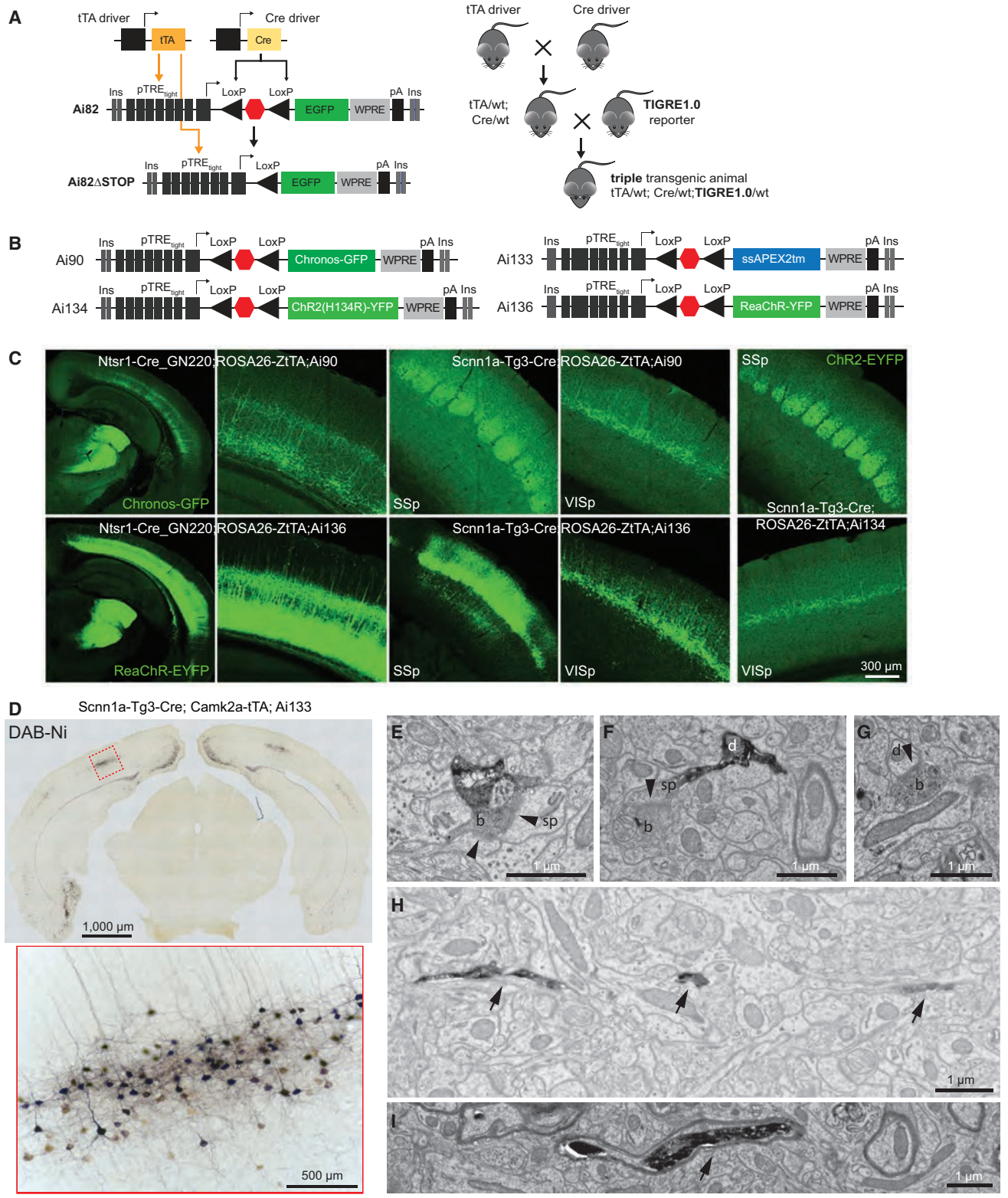

Figure 2. New TIGRE1.0 Reporter Lines for Optogenetics and Ultrastructural Labeling

(A) Cre- and tTA-dependent intersectional TIGRE1.0 reporter line design and generalized triple transgenic breeding scheme.

(B) Configurations of four new TIGRE1.0 reporter lines.

(legend continued on next page)

and found that they indeed label predominantly excitatory neurons in a layer-specific manner, with some lines also labeling some inhibitory interneuron populations (Figure 1B). We also characterized the eight driver lines expressing the DHFR-domain-containing dCre, dgCre, or dgFlpO. Recombinases fused to the destabilizing DHFR domain (Sando et al., 2013), which can be stabilized by the administration of an antibiotic TMP, constitute a safer alternative inducible recombinase system compared to CreERT2, whose requirement of tamoxifen dosing can lead to undesired side effects. We examined the recombination patterns of DHFR-containing driver lines in the adult stage without or with TMP induction (Table S3) and found substantial variability in baseline and induced states across different lines, suggesting that such characterization is critical for the proper use of these types of lines.

New Rosa26 and TIGRE1.0 Reporter Lines

We first summarize a set of Rosa26-based Cre reporter lines we generated but have not formally reported previously (Figure S1A; Table S2). These include Ai31 (with synapse-localized Synaptophysin-EmGFP), Ai34 (with synapse-localized Synaptophysin-tdTomato), Ai40 (with archeorhodopsin ArchT-GFP), Ai47 (with three tandemly linked GFP molecules EmGFP-T2A-TagGFP2-P2A-hrGFP), Ai75 (with nuclear-localized nls-tdTomato), Ai80 (a Cre and Flp double reporter with channelrhodopsin CatCh) (Kleinlogel et al., 2011), Ai86 (with voltage sensor ArcLight) (Jin et al., 2012), and Ai110 (a Cre and Flp dual reporter expressing nuclear-localized nls-mNeonGreen when only Cre is present and nls-tdTomato when both Cre and Flp are present). All of these lines display appropriate reporter gene expression when crossed to various Cre lines (Figures S1B–S1E).

We also generated a knock-in Chrm2-tdT line, in which tdTomato was fused to the C terminus of the endogenous muscarinic acetylcholine receptor 2 (*Chrm2*) gene (Figure S1A). Immunostaining of CHRM2 can be used to delineate cytoarchitectonic boundaries of various cortical areas (such as primary visual and somatosensory cortices) (Ji et al., 2015). We find that such delineation is preserved by native fluorescence of the CHRM2-tdTomato fusion in Chrm2-tdT mice (Figure S1F); thus, this line can be used to visualize cortical area boundaries *in vivo*.

We created a Flp-reporter line, Ai65F, and a Dre-reporter line, Ai66R (Figure S1A), by performing EIIa-Cre-mediated germline deletion of the Lox-STOP-Lox (LSL) cassette from our previously reported, Rosa26-based double reporter line of Cre and Flp, Ai65, and of Cre and Dre, Ai66, respectively (Madisen et al., 2015). Similarly, we created a tTA-reporter line Ai63 (Figure S1A) from the TIGRE-based Cre and tTA double reporter line Ai62. Expected specificity for their respective driver lines was observed (Figures 1A and S1G).

We generated several additional TIGRE1.0 lines (Figure 2A) expressing new tools. These include Ai90 (with channelrhodopsin Chronos-GFP) (Klapoetke et al., 2014), Ai133 (with an electron microscopy tag ssAPEX2tm) (Lam et al., 2015), Ai134 (with channelrhodopsin ChR2(H134R)-YFP), and Ai136 (with channelrhodopsin ReaChR-YFP) (Lin et al., 2013) (Figure 2B). In the required triple-transgenic setting (Cre x tTA x reporter), we found that the use of a moderately expressing tTA line, ROSA26-ZtTA (Li et al., 2010), led to good opsin expression when combining Ai90, Ai134, or Ai136 with cortical layer 4- or 6-specific Cre lines (Scnn1a-Tg3-Cre or Ntsr1-Cre_GN220) (Figure 2C). On the other hand, the use of a strong tTA driver, Camk2a-tTA, led to fluorescent aggregates in cells and/or aberrant morphology of labeled cells (data not shown), indicating adverse effects of overexpression of these opsin proteins.

Ai133 expresses ascorbate peroxidase APEX2 (Lam et al., 2015) tagged with a T cell CD2 antigen signal sequence (ss) and a transmembrane targeting sequence (tm), which we found to be compatible with transcardial perfusion and fixation with glutaraldehyde—a necessary step toward obtaining ultrastructure preservation for electron microscopy (EM). Incubation of coronal slices from Scnn1a-Tg3-Cre;Camk2a-tTA;Ai133 animals with 3,3′-diaminobenzidine enhanced with nickel (DAB-Ni) showed specific peroxidase activity in cortical layer 4 as expected (Figure 2D). Processing DAB-Ni stained tissue with a reduced osmium tetroxide (ROTO) protocol provided strong EM contrast and identification of APEX2-positive cell processes (Figures 2E–2I).

TIGRE2.0 Reporter Lines with Enhanced Expression

The TIGRE1.0 lines rely on two drivers for cell-type-specific and high-level transgene expression (Madisen et al., 2015) (Figure 2A). This triple transgenic design is limited by the availability of only a few well-functioning tTA lines. We previously observed robust transgene expression in cortical excitatory neurons and a subset of cortical interneurons or subcortical neurons but poor expression in many other neuronal types. To overcome this problem and to simplify breeding, we investigated ways to incorporate tTA-mediated transcriptional amplification into the TIGRE locus itself along with the reporter transgene (see Figure S2 legend).

We co-inserted two complete transgene-expressing units, separated by tandem HS4 insulators to mitigate potential interference between the two units, into the same TIGRE locus (Figure 3A). The first unit contains TRE2 promoter-driven, LSL-controlled reporter gene (e.g., GFP), and the second unit contains CAG promoter-driven, LSL-controlled tTA2 gene (or tdTomato-P2A-tTA2). We named this approach TIGRE2.0. In the presence of Cre, both STOP signals would be excised,

(C) Robust Cre/tTA-dependent expression of opsins in cortical layer 6 and 4 neurons.
(D) APEX2 activity revealed by DAB-Ni staining. Bright-field images reveal staining within somatic, dendritic, and axonal compartments of neurons located in several cortical regions, including layer 4 of VISp (enlarged image).
(E–G) Electron micrographs show APEX2-dependent labeling of both pre- and post-synaptic terminals. Examples include synapses (arrowheads) between a labeled bouton (b) and an unlabeled spine (sp) (E), between a labeled bouton and a labeled spine (F), and between a labeled bouton and an unlabeled dendritic shaft (d) (G).
(H and I) Electron micrographs show APEX2-dependent labeling of fine, unmyelinated (H) or myelinated (I) axons (arrows).
See also Table S2 and Figure S1.

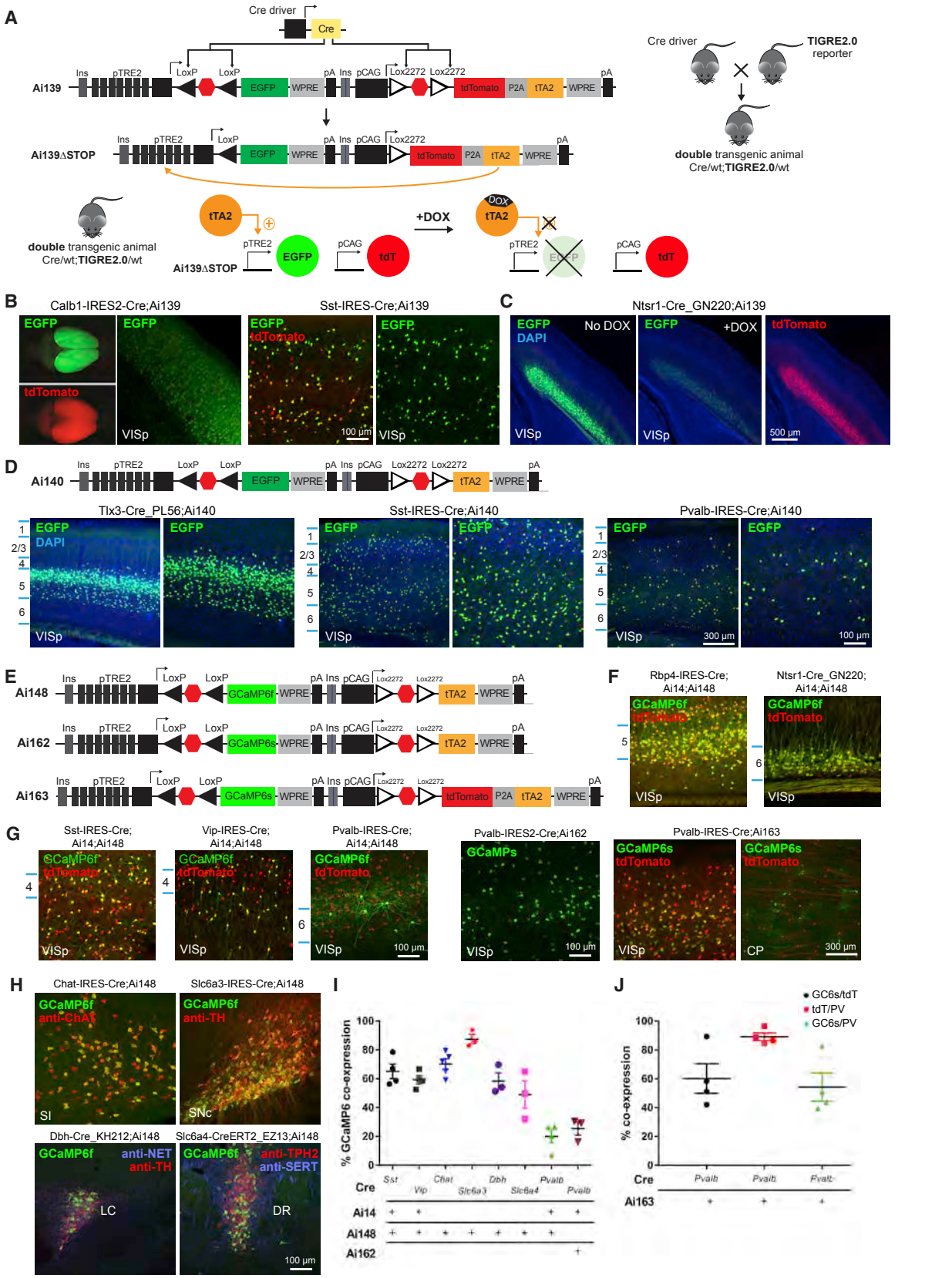

(legend on next page)

thereby allowing CAG promoter to drive tTA2 expression, which would in turn activate the reporter gene expression.

We developed two prototype TIGRE2.0 lines expressing GFP: Ai139(TIT2L-GFP-ICL-TPT) (stands for TIGRE-insulators-TRE2 promoter-LoxPStop1LoxP-GFP-insulators-CAG promoter-Lox2272Stop2Lox2272-tdTomato-P2A-tTA2) and Ai140(TIT2L-GFP-ICL-tTA2) (Figures 3A and 3D). To determine whether tTA2 expression from within the TIGRE locus is sufficient, we crossed these two lines to several Cre lines and examined GFP expression in a variety of cell types. In all cases, we observed strong native GFP fluorescence throughout cortical and subcortical areas (Figures 3B, 3D, and S2A), including *Pvalb*+ and *Sst*+ interneurons for which poor expression had been seen in TIGRE1.0 lines. Reporter expression could be reversibly suppressed by doxycycline (Figure 3C).

A Suite of TIGRE2.0 Reporter Lines Expressing Functional Probes in Diverse Cell Types

We proceeded to generate a set of TIGRE2.0 lines expressing other genetic tools for probing neural function. These include genetically encoded calcium indicators GCaMP6f and GCaMP6s (Figure 3E), new channelrhodopsin variants ChrimsonR (Klapoetke et al., 2014) and oChIEF (Ting et al., 2014), new genetically encoded voltage indicator ASAP2s (Chamberland et al., 2017; Yang et al., 2016) (Figure 4A), and a new Cre and Dre intersectional reporter line (Figure S2B).

We generated three TIGRE2.0 reporter lines expressing GCaMP6f or GCaMP6s: Ai148(TIT2L-GC6f-ICL-tTA2), Ai162 (TIT2L-GC6s-ICL-tTA2) and Ai163(TIT2L-GC6s-ICL-TPT) (Figure 3E). To compare with Rosa26-based reporters, we generated triple transgenic mice containing both Ai14 and Ai148 along with one of five Cre lines. With cortical layer-specific Cre lines (Figure 3F), we observed near-complete overlap between GCaMP6f+ and tdTomato+ cells. With the three cortical interneuron-specific Cre lines (Figure 3G), GCaMP6f and tdTomato were largely co-expressed, but we also detected cells expressing only tdTomato, indicating that the difficulty of achieving tTA-dependent expression in interneuron populations is not fully overcome. This is particularly the case for *Pvalb*+ interneurons, which had the lowest proportion of GCaMP6f+ cells relative to tdTomato+ cells. On the other hand, we observed robust GCaMP6s expression in many *Pvalb*+ cells when crossing Ai162 or Ai163 with Pvalb-IRES-Cre (Figure 3G). Quantification confirmed that GCaMP6s was expressed in a larger (in Ai162) or substantially larger (in Ai163) portion of *Pvalb*+ cells than GCaMP6f (in Ai148) (Figures 3I and 3J).

We investigated Ai148 GCaMP6f expression in subcortical neuromodulatory neurons by quantifying the fraction of cells expressing GCaMP6f driven by corresponding Cre lines in cholinergic, dopaminergic, noradrenergic, and serotoninergic neurons identified by immunohistochemistry (IHC) (Figures 3H, 3I, S3A, and S3B). A large fraction of neuromodulatory neurons displayed strong native GCaMP6f fluorescence without IHC enhancement. This is a substantial improvement over previous generations of both Rosa26 and TIGRE1.0 GCaMP6 reporter lines, in which GCaMP6 fluorescence was virtually undetectable in neuromodulatory neurons, shown as an example in the cholinergic neurons (Figures S3C and S3D).

We generated two TIGRE2.0 lines expressing new opsins: Ai167(TIT2L-ChrimsonR-tdT-ICL-tTA2) and Ai168(TIT2L-oChIEF-P2A-tdT-ICL-tTA2) (Figure 4A). In *Cux2*+ cortical layer 2/3 neurons, strong membrane fluorescence for the ChrimsonR-tdTomato fusion protein was observed (Figure 4B). In this case, we also show that TIGRE2.0 lines can be combined with TIGRE1.0 lines to achieve dual expression of two reporter genes from a single Cre-dependent tTA2 expression unit, as seen in Cux2-CreERT2;Ai93;Ai167, in which both ChrimsonR-tdT (from Ai167) and GCaMP6f (from Ai93) were expressed in the same or different Cre+ cells. In Ai168, oChIEF, specifically oChIEF$_{AC}$, was expressed singly and not fused to a fluorescent protein, so its expression was revealed by immunostaining using an antibody against the 2A peptide, and it coincided well with the tdTomato fluorescence (Figure 4C).

We generated two TIGRE2.0 lines expressing a voltage sensor ASAP2s: Ai169(TIT2L-ASAP2s-ICL-tTA2) and Ai170 (TIT2L-ASAP2s-Kv-ICL-tTA2), in which ASAP2s is tagged with a 65-amino-acid cytosolic segment of Kv2.1 to restrict protein localization to the soma and proximal dendrites (Baker et al., 2016; Lim et al., 2000; Wu et al., 2013) (Figure 4A; Table S4). Both lines exhibit robust fluorescence with expected localizations—membrane-localized throughout neuronal processes for ASAP2s in Ai169 and soma-enriched for ASAP2s-Kv in Ai170 (Figure 4D).

Figure 3. TIGRE2.0 Lines Display Enhanced Expression in a Wide Range of Cell Types

(A) Cre-dependent TIGRE2.0 reporter line design and simplified double transgenic breeding scheme. The tTA2 activity and subsequent TRE2 promoter-driven expression can be suppressed by giving doxycycline (DOX) to double transgenic mice.

(B) Representative images of native EGFP and tdTomato fluorescence in VISp of Cre;Ai139 double transgenic mice.

(C) Representative images of native EGFP and tdTomato fluorescence in VISp of Ntsr1-Cre_GN220;Ai139 mice with or without DOX.

(D) Configuration of Ai140 and representative images of native EGFP fluorescence in VISp from Cre;Ai140 mice.

(E) Configurations of GCaMP6-expressing TIGRE2.0 reporter lines.

(F) Representative images of native GCaMP6f and tdTomato fluorescence in Cre;Ai14;Ai148 mice demonstrate layer-specific expression patterns.

(G) Representative images of native GCaMP6 and tdTomato fluorescence in major inhibitory neuron classes of indicated triple or double transgenic mice.

(H) Co-localization of native GCaMP6f fluorescence and immunostaining for major neuromodulatory markers in corresponding Cre;Ai148 mice (anti-ChAT for cholinergic, anti-TH for dopaminergic, anti-NET and anti-TH for noradrenergic, and anti-TPH2 and anti-SERT for serotoninergic neurons). For region acronyms, see STAR Methods.

(I) Quantification of GCaMP6-expressing cells in Cre-defined cell classes. For cortical interneuron classes (*Sst*, *Vip*, and *Pvalb*), native GCaMP6 co-expression with tdTomato (from Ai14) was quantified within VISp and expressed as a percentage of the number of tdTomato+ cells. For neuromodulatory neuron types, native GCaMP6f co-expression with the indicated cell-type-specific markers in (H) was expressed as a percentage of the number of marker-positive cells. Data are presented as mean ± SEM (same in [J]); n = 3–5 mice.

(J) Quantification of GCaMP6s and tdTomato co-expression in *Pvalb*+ (anti-PVALB labeled) cells of Pvalb-IRES-Cre;Ai163 mice (n = 3–4).

See also Table S2 and Figures S2 and S3.

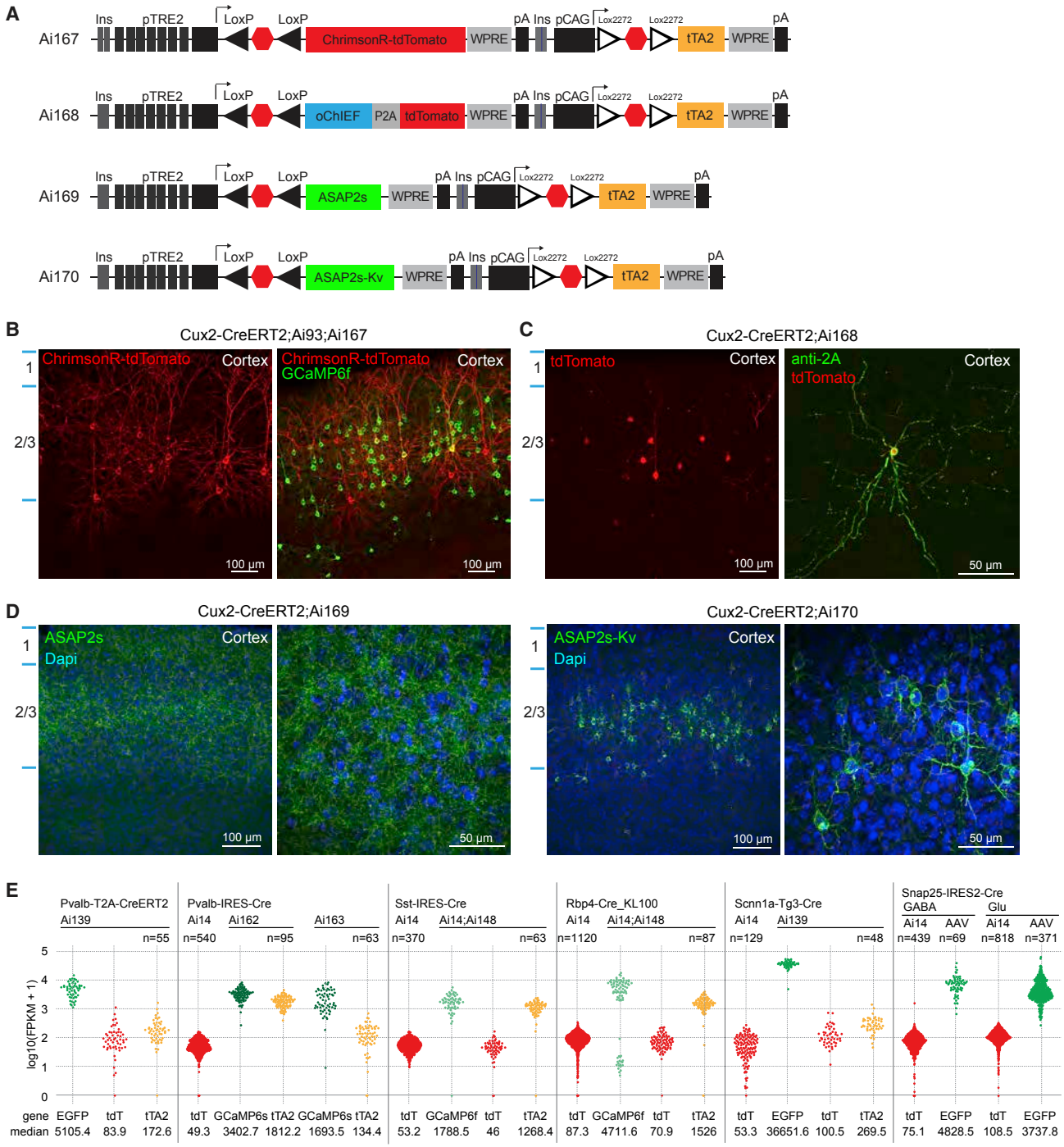

Figure 4. TIGRE2.0 Reporter Lines Exhibit High-Level Transgene Expression

(A) Configurations of opsin or voltage indicator expressing TIGRE2.0 reporter lines.

(B) Representative images of native ChrimsonR-tdT and GCaMP6f fluorescence in a Cux2-CreERT2;Ai93;Ai167 mouse with low-dose tamoxifen induction.

(C) Expression of oChIEF as visualized by anti-2A peptide staining and its co-localization with tdTomato in a Cux2-CreERT2;Ai168 mouse.

(D) Representative images of native ASAP2s and ASAP2s-Kv fluorescence in Ai169 and Ai170 crossed to Cux2-CreERT2.

(E) Quantification of mRNA levels of reporter transgenes by single-cell RNA sequencing (scRNA-seq). Normalized expression values are shown for each cell as fragments per kilobase per million reads (FPKM). Transgene expression levels in cells isolated from various Cre x TIGRE2.0 mice or from AAV injected mice were compared with control cells from corresponding Cre x Ai14 mice. Snap25-IRES2-Cre;Ai14 and Snap25-IRES2-Cre AAV cells were separated into glutamatergic (Glu) and GABAergic (GABA) groups for comparison.

See also Figure S4 and Table S4.

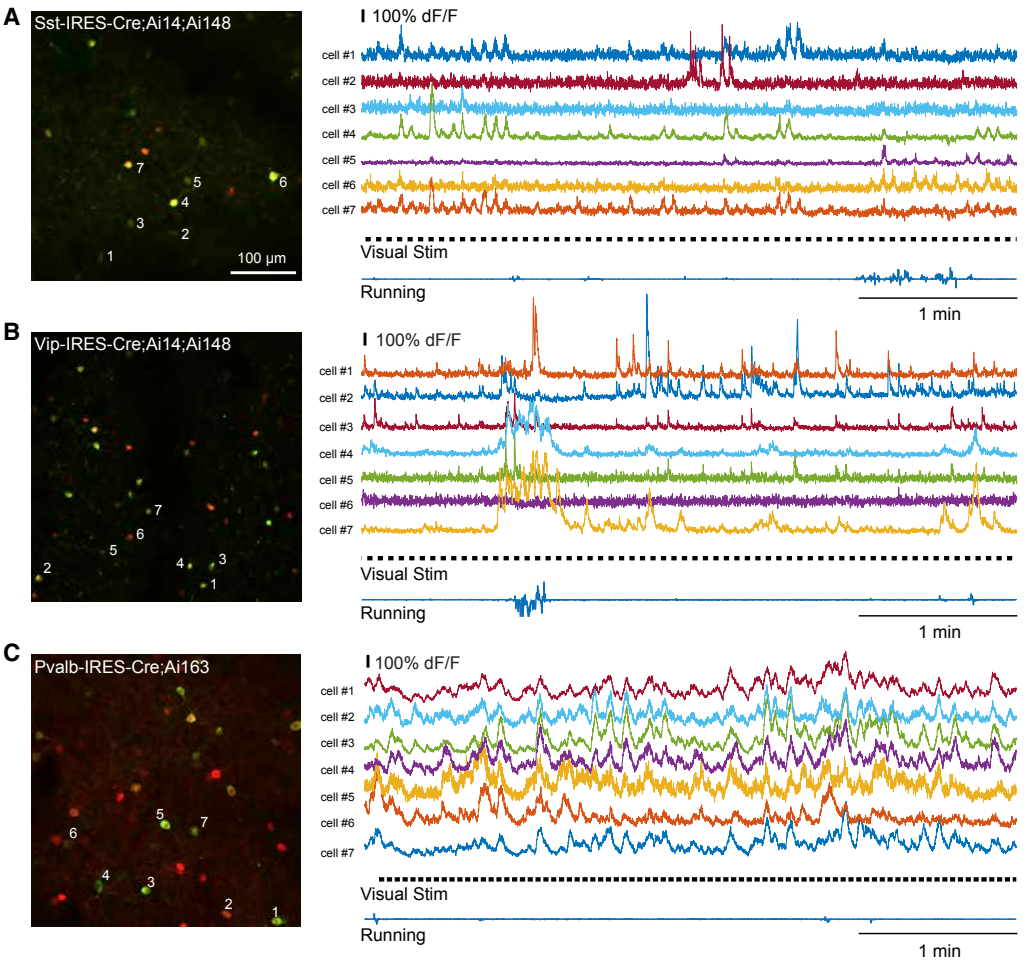

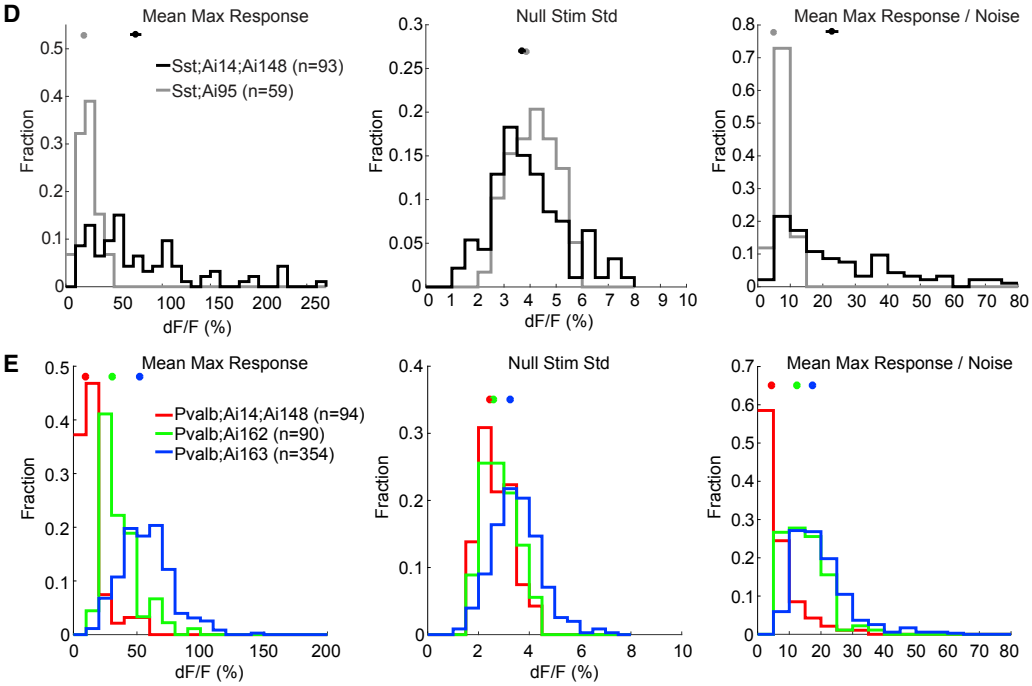

(legend on next page)

To quantitatively evaluate transgene expression levels in TIGRE2.0 lines, we isolated individual cells from different mouse lines by fluorescence-activated cell sorting (FACS) and performed single-cell RNA sequencing using the SMART-Seq v4 method (Tasic et al., 2016) (Figure 4E). In all inhibitory and excitatory neuronal types examined, TRE2 promoter-driven reporter levels of GFP in Ai139, GCaMP6f in Ai148, and GCaMP6s in Ai162 or Ai163 were 40- to 400-fold higher than CAG promoter-driven tdTomato levels in Ai14 or Ai139. We also noted that tTA2 levels were significantly higher when expressed alone (in Ai148 and Ai162) than in the tdT-P2A-tTA2 configuration (in Ai139 and Ai163); however, this did not translate into higher TRE2-driven reporter levels, indicating a saturation had been reached. We further found that TIGRE2.0 reporter gene levels were comparable to the GFP expression level from excitatory or inhibitory neurons 3–5 weeks after infection with a very strong, Cre-dependent adeno-associated viral vector, AAV-pCAG-FLEX-EGFP-WPRE-pA (Figure 4E), suggesting that strong viral-like expression level has been achieved in TIGRE2.0 lines.

To assess the effect of high-level transgene expression, we examined transcriptome-wide changes by comparing the single-cell transcriptomes from the above Cre x TIGRE2.0 mice to those from matching classes of cells from Cre x Ai14 mice and found no substantial changes in global gene expression (Figure S4). We also found that a group of immune-responsive genes were substantially upregulated in AAV-infected cells but not in TIGRE2.0 cells.

In Vivo Calcium Imaging In Cortical Neurons Using TIGRE2.0 GCaMP6 Reporters

To evaluate the utility of TIGRE2.0 mice in studying cortical interneurons, *in vivo* two-photon (2P) calcium (Ca) imaging was conducted in triple transgenic mice containing Ai14 and Ai148 reporters and one of the Cre lines specific for *Pvalb*, *Sst*, or *Vip* interneurons. Co-expressing tdTomato with GCaMP6f facilitated the localization of and Ca imaging in those interneurons with low neural activity or fluorescence (Figure 3G).

2P Ca imaging was conducted in layer 2/3 (110–350 μm below the pia) through an implanted cranial window over the left primary visual cortex (VISp) in head-fixed, awake mice. Ca imaging with drifting gratings (Figures 5 and S5A–S5D) confirmed that Ai148/162/163 mice greatly improved the expression of GCaMP6 in interneurons with high specificity, compared to the absent or low expression in corresponding Ai93/Ai95 mice (Madisen et al., 2015). Sst-IRES-Cre;Ai14;Ai148 mice showed large evoked fluorescence changes (ΔF/F) in response to drifting gratings and a great degree of variation of baseline and visually evoked fluorescence. Large responses were also seen in Vip-IRES-Cre;Ai14;Ai148 mice, and the behavioral state (running versus stationary) dependency was well evident. In Pvalb-IRES-Cre;Ai14;Ai148 mice, the number of GCaMP6f-expressing cells was small and Ca response was low. Thus, we also performed *in vivo* 2P Ca imaging in Pvalb-IRES-Cre;Ai162 and Pvalb-IRES-Cre;Ai163 mice, in which we observed much stronger spontaneous and visually evoked responses.

To quantify the improvement of Ai148 over Ai95, we compared the fluorescence responses of cells in Sst-IRES-Cre;Ai14;Ai148 mice (two mice, eight fields of view [FOVs]) with those in Sst-IRES-Cre;Ai95 (two mice, six FOVs) (Figure 5D). To control for imaging noise, we calculated the mean maximum response of individual cells by taking the maximal ΔF/F response averaged within 1 s (0.5–1.5 s) post-stimulus onset during the entire recording episode. Compared with Ai95, the distribution of mean maximum responses in Ai148 showed a significant rightward shift ($p < 0.001$, Kolmogorov-Smirnov test). The average amplitude of Ai148 response was larger (72.45% ± 5.88% ΔF/F, mean ± SEM, same below) than that of Ai95 (18.93% ± 1.18%, $p < 0.001$, t test). The noise level (3.69% ± 0.15% ΔF/F) in Ai148 remained comparable with that in Ai95 (3.86% ± 0.11%, $p = 0.37$, t test). Thus, Ai148 had significantly increased signal/noise ratio by ~4-fold (22.84 ± 1.96 versus 4.94 ± 0.31, $p < 0.001$, t test).

Strong fluorescence responses were also observed in GCaMP6s-expressing Ai163 and Ai162 lines. In Pvalb-IRES-Cre;Ai163 (three mice, 18 FOVs), for example, responses in *Pvalb* neurons were on average ~5-fold (52.39% ± 1.05% ΔF/F) greater than those of Pvalb-IRES-Cre;Ai14;Ai148 (9.74% ± 1.10%, two mice, six FOVs; $p < 0.001$, t test) (Figure 5E). Although the baseline noise was higher (3.26% ± 0.05% versus 2.46% ± 0.07%, $p < 0.001$, t test) due to the high activity level of *Pvalb* neurons *in vivo* and increased sensitivity in Ai163, overall the signal-to-noise ratio significantly increased by ~4-fold compared with Ai148 (17.42 ± 0.47 versus 4.48 ± 0.56, $p < 0.001$, t test, Figure 5E).

To also assess the utility of Ai148 for imaging excitatory neurons, we crossed Ai148 with Cre-lines targeting deep cortical layers. Ntsr1-Cre_GN220;Ai148 mice expressed GCaMP6f strongly and specifically in layer 6 across the cortex (Figure S5E), while Ntsr1-Cre_GN220;Camk2a-tTA;Ai93 mice displayed less specificity, with strong expression in some layer 5 cells as well (Figure S5F). While imaging in VISp layer 6, both sets of mice showed strong visually evoked responses to drifting gratings (Figures S5E and S5F). Comparison of the distribution of response amplitudes showed larger changes in fluorescence in

Figure 5. *In Vivo* 2P Calcium Imaging in Cortical Neurons with TIGRE2.0 GCaMP6 Mice

(A) 2P Ca imaging of Sst;Ai14;Ai148 neurons. Left: Z-projection image (time series) showing the entire field of view (400 × 400 μm) at 212 μm below the pial surface. Right: ΔF/F traces for 250 s of imaging in seven *Sst* neurons as labeled in the left panel. Time course of visual stimuli and running velocity was also shown. Same for (B) and (C).

(B) 2P Ca imaging of Vip;Ai14;Ai148 neurons at 192 μm depth. Note that the fluorescence change started before the initiation of running.

(C) 2P Ca imaging of Pvalb;Ai163 neurons at 280 μm depth.

(D) Improved functionality of GCaMP6f in *Sst* cells in Ai148 relative to Ai95, as shown in population histograms of mean max responses (left), standard deviation of ΔF/F during gray screens (null stimuli, middle), and estimated signal-to-noise ratio (right).

(E) Comparison of GCaMP6 functionality in *Pvalb* cells in Ai148, Ai162, and 163 mice.

See also Figure S5.

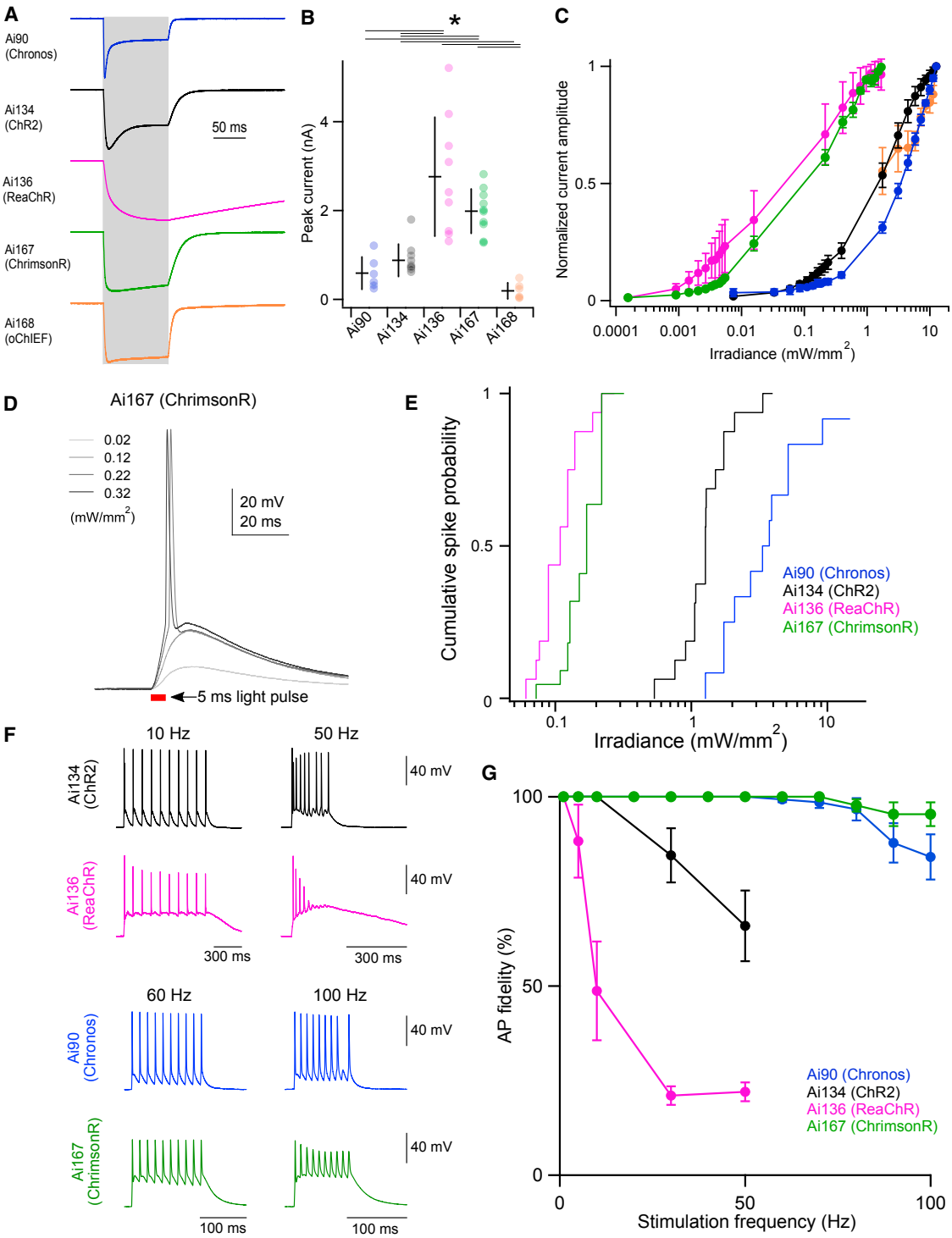

Figure 6. Characterization of Light-Evoked Responses in Opsin-Expressing TIGRE1.0 and TIGRE2.0 Lines

Mouse lines examined are Scnn1a-Tg3-Cre;ROSA26-ZtTA;Ai90 (simplified as Scnn1a-Ai90 or Ai90, same below), Scnn1a-Tg3-Cre;ROSA26-ZtTA;Ai134, Scnn1a-Tg3-Cre;ROSA26-ZtTA;Ai136, Scnn1a-Tg3-Cre;Ai167, and Scnn1a-Tg3-Cre;Ai168.

(A) Representative examples of light-evoked currents in response to 100 ms stimulation (indicated by gray shading). Traces are from individual neurons and are normalized to their peak current amplitude.

(B) Average ± SD of peak current amplitude and data points for individual cells from each transgenic line. Ai90: 0.59 ± 0.36 nA; Ai134: 0.88 ± 0.36 nA; Ai136: 2.76 ± 1.34 nA; Ai167: 1.99 ± 0.50 nA; Ai168: 0.19 ± 0.18 nA. *$p < 0.005$ ($n = 6–10$ cells for each line).

(legend continued on next page)

Ai93, both when recording in layer 6 (Ntsr1-Cre_GN220 in Figure S5G averaged 25% ± 3% ΔF/F in Ai93, n = 183 cells, and 12% ± 1% in Ai148, n = 310 cells) and in layer 5 (Tlx3-Cre_PL56 in Figure S5H; 20% ± 5% ΔF/F in Ai93, n = 281 cells, and 12% ± 1% in Ai148, n = 349 cells). However, many more GCaMP6f+ cells were detected with Ai148 overall in both excitatory populations, suggesting that this reporter may have detected more cells with no or low evoked activities.

Light-Response Properties of TIGRE1.0 and TIGRE2.0 Optogenetic Mice

We characterized the light responses of the three new TIGRE1.0 lines and two new TIGRE2.0 lines expressing various channelrhodopsin variants in acute slices of VISp. Recordings were targeted to opsin-positive neurons in layer 4. We stimulated neurons from Ai90, Ai134, and Ai168 mice using a blue LED (470 nm). The reported photo-activation spectra of ReaChR and ChrimsonR are red shifted compared to ChR2 (Klapoetke et al., 2014; Lin et al., 2013); therefore, we utilized a red-orange LED (590 nm) to stimulate cells in Ai136 and Ai167 mice.

As observed in the initial description of each opsin, the photocurrents carried by these five variants demonstrate distinct kinetics (Figure 6A). Photocurrents from Chronos+ cells (Ai90) displayed the most rapid kinetics with a sub-millisecond time constant of activation (Figure S6A). By comparison, activation kinetics were slightly slower in oChIEF+ (Ai168), ChrimsonR+ (Ai167), and ChR2+ (Ai134) neurons and dramatically slower in ReaChR+ (Ai136) neurons. We also observed similar pattern in deactivation kinetics for these opsins (Figure S6B). Chronos and ChR2 photocurrents both displayed significant desensitization over the course of a 100 ms stimulus, while desensitization was significantly lower for oChIEF or ChrimsonR and absent in ReaChR (Figure S6C).

Ai167 exhibited large-amplitude ChrimsonR-mediated photocurrents (Figure 6B: peak current amplitude = 1.99 ± 0.50 nA, n = 10). By contrast, Ai168 oChIEF-mediated photocurrents were an order of magnitude smaller. Among the three TIGRE1.0 lines tested, Ai136 peak current amplitudes were comparable to Ai167, while Ai134 and Ai90 were significantly smaller. To compare variability of opsin expression within transgenic lines, we measured the coefficient of variation (CV) of the peak current amplitudes between cells. Notably, Ai167 displayed the smallest CV (CV = 0.25; compared to CV = 0.62, 0.42, 0.48, and 0.93 for Ai90, Ai134, Ai136, and Ai168, respectively), suggesting that the Ai167 line provides robust and consistent opsin expression from cell to cell. We compared photosensitivity by measuring currents across a range of light intensities (Figure 6C). All five lines displayed strong sensitivity to light intensity with the greatest sensitivity seen in Ai167 and Ai136.

Generation of light-evoked action potentials (APs) was highly reliable in all effector lines except Ai168, in which optically evoked APs were observed only in a minority of cells tested (Figure S6D). To compare the capacities of the remaining effector lines to produce optically evoked APs, we measured depolarizations in response to a 5 ms optical stimulus of increasing power (Figure 6D). From these, we determined the minimum power necessary to generate APs and plotted cumulative spike probability versus light intensity for the four lines (Figure 6E). Very low powers were required to produce APs in ChrimsonR (Ai167: 0.07–0.32 mW/mm^2, median = 0.17 mW/mm^2) or ReaChR cells (Ai136: 0.06–0.27 mW/mm^2, median = 0.11 mW/mm^2). Chronos and ChR2 cells required 10- to 30-fold higher powers to evoke APs (Ai90: 1.3–14.5 mW/mm^2; median = 3.5 mW/mm^2; Ai134: 0.53–3.9 mW/mm^2; median = 1.3 mW/mm^2). While the required powers are significantly larger, they are readily achievable with commonly utilized light sources, and we observed spiking in all ChR2 neurons (n = 16) and all but one Chronos neuron (n = 13; Figure S6D). ChR2 and Chronos neurons were excited with a blue (470 nm) LED—slightly shorter than the reported excitation peak of Chronos (500 nm) (Klapoetke et al., 2014). Use of a light source tailored to Chronos would likely provide robust spiking at even lower powers. These data correspond well with our direct recordings of opsin-mediated currents (compare Figure 6C to 6E).

We next utilized light pulses of saturating intensity to determine the minimum duration of light exposure necessary to elicit APs in each effector line (Figure S6E). Minimum durations of exposure were below 0.5 ms in nearly all neurons tested, and Ai167 and Ai136 were the most responsive—all cells exhibited minimum duration of exposure $\leq$0.12 ms (Figure S6F). We also presented opsin-expressing neurons with 1 ms light pulses of saturating intensity and measured the average latency of AP firing and the jitter (standard deviation of the latency) associated with this common stimulus. All four lines displayed highly precise firing with average jitters <0.1 ms. ChrimsonR neurons (Ai167) had the lowest latency and jitter (Figures S6G and S6H). Similar to results obtained from the Scnn1a-Tg3-Cre cross, ChrimsonR cells displayed robust and reliable spiking in response to photostimulation in layer 2/3 neurons of Cux2-CreERT2;Ai167 mice (Figures S6F–S6H).

Finally, we measured the fidelity of optically evoked AP firing in response to ten repeated stimuli of increasing frequency (Figures 6F and 6G). Consistent with the slow kinetics of channel activation and deactivation, ReaChR cells (Ai136) displayed the least reliable firing in response to high-frequency stimuli. ChrimsonR (Ai167) and Chronos (Ai90) both exhibited a remarkable ability to follow optical stimuli delivered up to 50 Hz. In attempt to better differentiate the two lines, we delivered additional stimuli at

(C) Power-dependence of photocurrent activation for each transgenic line. Data are plotted as mean ± SD. Current amplitudes evoked by powers <1 mW/mm^2 in the Ai168 line were not quantified due to their low amplitude.
(D) Representative responses of a Scnn1a-Tg3-Cre;Ai167 cell to 5 ms light pulses of increasing power.
(E) Cumulative spike probability plotted against photostimulation power for each transgenic line.
(F) Comparison of high-frequency firing between transgenic lines. Representative voltage recordings from individual cells in response to ten repeated stimuli at the indicated frequencies.
(G) Plot of AP fidelity versus stimulus frequency for each transgenic line. Data are plotted as the mean ± SEM (n = 9–15 cells for each line).
See also Figure S6.

frequencies ranging from 60 to 100 Hz. AP fidelity was near 100% for both lines and population averages were not significantly different from each other. However, as can be appreciated from the example traces, stimulation of Ai167 neurons at very high frequencies led to AP broadening and shortening that was not seen in Ai90 (Figure 6F). Altogether, our analyses of photocurrents and optically evoked depolarizations across these transgenic lines suggest that they together provide a powerful and complementary toolset for a variety of optogenetic experiments.

Assessment of Adverse Effects Associated with Extremely High-Level Transgene Expression

Very high transgene expression achieved with either viral or transgenic approaches may cause unwanted phenotypes (Han et al., 2012), and therefore, one should always be cautious and carefully evaluate cell health in each experimental context. While for the vast majority of Cre x TIGRE2.0 crosses examined (>50) the brains and labeled cells appeared healthy, we did observe some adverse effects in selected crosses (Figure S7; Table S5). For most of these cases, feeding the mice doxycycline-containing chow throughout the pregnancy and animal's lifetime did not ameliorate the adverse phenotypes (data not shown), suggesting that very high levels of tTA2, a potent transcriptional activator, are not well tolerated when broadly expressed in CNS, early in development and/or potentially outside of the CNS. We caution users against using Cre lines with widespread and early developmental expression and suggest using the more specific Cre lines in which we have not observed any adverse phenotypes.

We have recently reported the occurrence of aberrant cortical dynamics in some strains of GCaMP-expressing mice (Steinmetz et al., 2017). This is an example of more subtle effects with widespread and strong calcium indicator expression, which could be alleviated by doxycycline treatment, and we have developed methods to detect them. These events resemble the synchronized interictal discharges observed in the context of epilepsy and are characterized by their repetitive discharge (~0.5 Hz), large amplitude (>10%), brief duration (<200 ms in GCaMP6f, <500 ms in GCaMP6s), and a spatial extent that includes motor and somatosensory regions of cortex. Aberrant activity was typically observed in strains with widespread expression of GCaMP across cortex, in particular when GCaMP expression was driven by Emx1-Cre, e.g., the Emx1-IRES-Cre;Camk2a-tTA;Ai93 mice. To screen for the incidence of these events in TIGRE2.0 strains, we used wide-field calcium imaging through the intact skull (Figure 7; Table S6). We did not observe aberrant activity from GCaMP6s-expressing Slc17a7-IRES2-Cre;Ai162 mice, but we were able to detect events from GCaMP6f-expressing Slc17a7-IRES2-Cre;Ai148 mice. For comparison, we also found a low incidence of aberrant activity in Slc17a7-IRES2-Cre;Camk2a-tTA;Ai93 mice. Events resembled those from the original report (Steinmetz et al., 2017) and our consistent observations in Emx1-IRES-Cre;Camk2a-tTA;Ai93 mice (five consecutive positive observations in each of five mice, one example shown in Figure 7D). Our analysis indicates that mice with GCaMP6s expression rarely exhibited aberrant activity, with only one available example (Figure 7E) indicating that our analysis is able to detect these events when reported by the slow calcium indicator.

DISCUSSION

Our previous efforts established the TIGRE locus as a new permissive docking site for insertion of exogenous promoters and transgenes (Madisen et al., 2015). TIGRE1.0 Cre/tTA-dependent intersectional reporter lines demonstrated much enhanced expression level due to tTA-mediated transcriptional amplification. Currently, the availability of tTA driver lines is limited, and in our own several attempts to create new knock-in tTA (specifically, tTA2) driver lines, little to no expression was often observed, possibly due to the silencing effect at those endogenous gene loci. The CAG promoter-driven tTA2 expression in our TIGRE2.0 lines is largely resistant to silencing in nearly all the cell types we have examined, including those we failed to label using TIGRE1.0 lines, such as cortical interneurons and subcortical neuromodulatory neurons, resulting in further enhanced expression of reporter or effector genes that was never reported before. However, the labeling across some of these cell types is still not 100%, indicating that the strategy is not perfect yet and that silencing may still be an issue (Zhu et al., 2007).

The TIGRE2.0 platform offers several major improvements over the existing genetic approaches. First, by removing one exogenous driver (tTA), the breeding strategy is simplified to a Cre-dependent approach; it also makes room for the creation of more generally useful dual recombinase-based intersectional strategies such as Cre and Dre reporters (e.g., Ai161) and Cre and Flp reporters (to be generated). Second, as discussed above, by using the robust and ubiquitous CAG promoter to drive tTA2, more consistent and uniform expression of the reporter genes across many different cell types is achieved, minimizing another type of variation. Third, the success of using two different promoters in the TIGRE locus suggests that this locus is indeed universally permissive and that it may be used for hosting other promoters or regulatory elements as well.

While the TIGRE2.0 lines represent broadly useful tools for cell-type-specific analysis, there are limitations to their utility, as with many existing genetic tools. In general, tTA is a potent transcriptional transactivator that has been reported to cause neurodegeneration when expressed at high levels (Han et al., 2012); thus, it is not surprising that its strong expression could be detrimental. In this regard, it is interesting to note that Pvalb-IRES-Cre;Ai163 mice had a higher proportion of *Pvalb*+ cells expressing GCaMP6s and also larger *in vivo* GCaMP6s responses than Pvalb-IRES-Cre;Ai162 mice, even though the former (containing tdTomato-P2A-tTA2) expresses tTA2 at a lower level than the latter (containing tTA2 alone). This suggests to us that future improvements can be made by moderately reducing tTA2 expression level and/or by using less potent tTA variants.

Beyond tTA2, widespread and high-level expression of other transgenes could also lead to adverse effects. For example, GCaMP6f mice are more prone to having epileptiform activities than GCaMP6s mice. For the different opsin variants, cells appeared healthier when lower-expressing ROSA26-ZtTA was

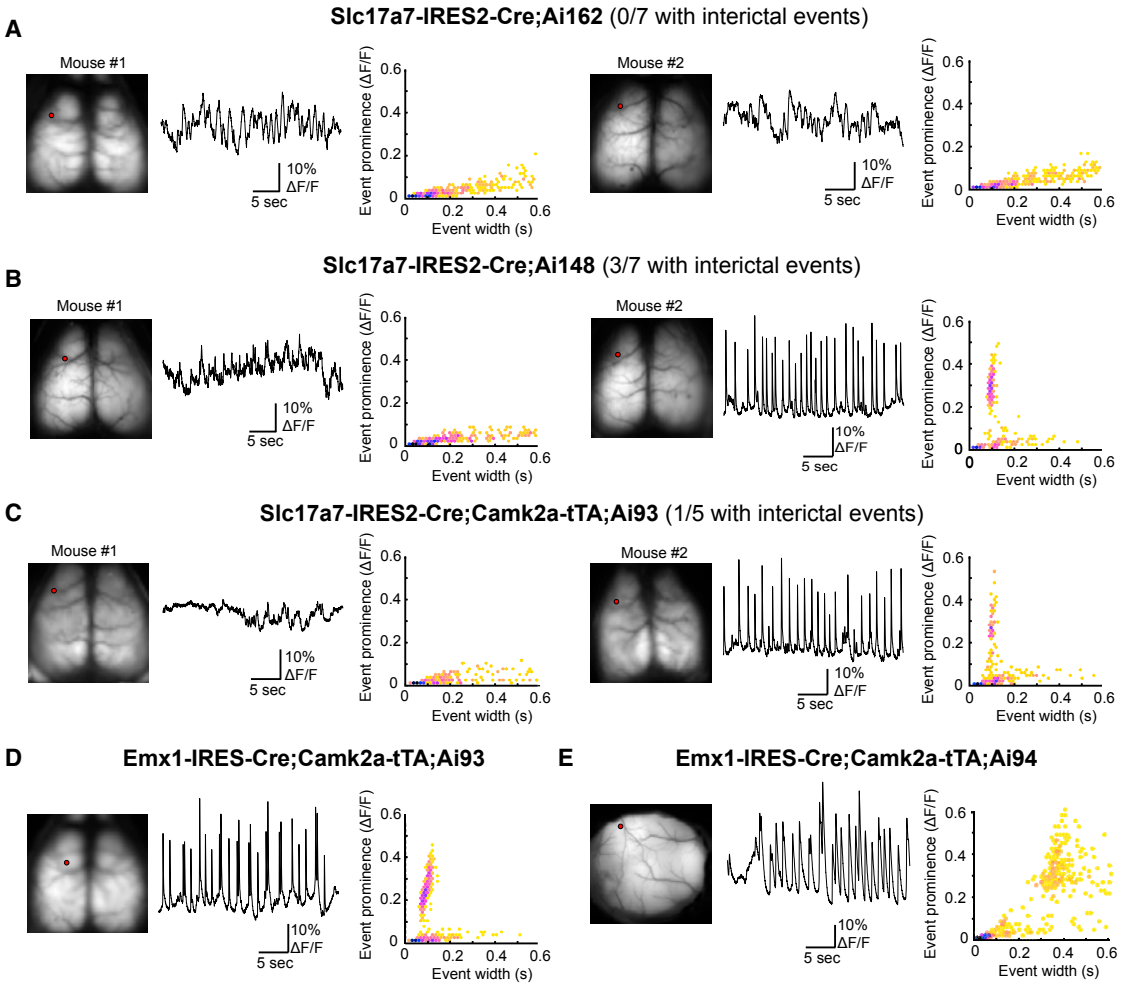

Figure 7. Incidence of Aberrant Cortical Activity in Mice with Cortical Pan-excitatory GCaMP6 Expression

Wide-field Ca imaging to examine interictal activities across the cortex. One or two representative examples are shown for each mouse line. For each mouse, left shows GCaMP6 fluorescence from the dorsal surface of the cortex, middle shows a 30 s example trace of calcium activity from a location in motor cortex (the red dot in the left), and right shows the relationship between event amplitude (prominence) and event width (hexagonally binned scatterplot).

(A) None of the seven Slc17a7-IRES2-Cre;Ai162 mice examined had aberrant activity.

(B) Aberrant activity was detected in three of seven Slc17a7-IRES2-Cre;Ai148 mice examined, one of which is mouse #2 shown on the right.

(C) Aberrant activity was detected in one of five Slc17a7-IRES2-Cre;Camk2a-tTA;Ai93 mice examined, and this is mouse #2 shown on the right.

(D) An example Emx1-IRES-Cre;Camk2a-tTA;Ai93 mouse that had aberrant activity.

(E) The only Emx1-IRES-Cre;Camk2a-tTA;Ai94 mouse we examined from this cross that exhibited aberrant activity (region shown is somatosensory cortex). Note the difference in event characteristics when reported by GCaMP6f (D) or GCaMP6s (E) indicator.

See also Figure S7 and Tables S5 and S6.

used compared to Camk2a-tTA to drive Chronos, ChR2, or ReaChR from TIGRE1.0 transgenes. On the other hand, it is interesting to note that ChrimsonR appears to be well tolerated even in the TIGRE2.0 configuration and exhibits high light sensitivity and high temporal precision. Thus, every molecule likely has its own optimal range of expression and will need to be treated differently to obtain a good balance between maximizing expression or functionality and minimizing toxicity. These conclusions will likely apply to the viral approaches as well. The large set of Rosa26-, TIGRE1.0-, and TIGRE2.0-based single-copy transgenic reporter mouse lines we generated has revealed a wide range of expression levels (from insufficient in some cases to "overkill" in others) for a diverse set of molecular tools. They also demonstrate that we now have the ability to fine-tune transgene expression levels as needed. The lessons learned here will be as important as the positive utility demonstrated to facilitate future development and utilization of optimal genetic targeting strategies.

Our overall results suggest that the diverse set of new driver and reporter lines reported here can enable numerous cell-type-specific applications. These include synaptic terminal labeling (Ai31 and Ai34); nuclear labeling (Ai75 and Ai110); *in vivo* visualization of anatomical structures (Chrm2-tdT); dendritic, axonal, and synaptic labeling under electron microscopy

(Ai133); full neuronal morphologies (Ai139, Ai140, and Ai161); cortical and subcortical *in vivo* calcium imaging of cell bodies as well as processes (Ai148, Ai162, and Ai163); *in vivo* voltage imaging (Ai86, Ai169, and Ai170); and one- or two-photon optogenetics (Ai40, Ai80, Ai90, Ai134, Ai136, and Ai167). Combined with the large arsenal of Cre, Flp, and other driver lines already existing or being generated based on single-cell transcriptome-identified cell types, and with complementary viral vectors that allow anterograde or retrograde labeling or systemic delivery, these applications can be carried out in dense, sparse, intersectional, or connectionally labeled cell populations for very refined circuit dissection, ultimately accelerating our understanding of brain functions in healthy or diseased conditions.

STAR★METHODS

Detailed methods are provided in the online version of this paper and include the following:

- KEY RESOURCES TABLE
- CONTACT FOR REAGENT AND RESOURCE SHARING
- EXPERIMENTAL MODEL AND SUBJECT DETAILS
  - Animal care and use
- METHOD DETAILS
  - Transgenic mice generation
  - Administration of trimethoprim or tamoxifen
  - *In situ* hybridization
  - Immunohistochemistry and imaging
  - Electron Microscopy
  - Single-cell RNA-sequencing
  - *In vivo* two-photon calcium imaging in cortical interneurons
  - *In vivo* two-photon calcium imaging in cortical excitatory neurons
  - Acute slice physiology and optogenetics
  - Wide-field calcium imaging
- QUANTIFICATION AND STATISTICAL ANALYSIS
- DATA AND SOFTWARE AVAILABILITY

SUPPLEMENTAL INFORMATION

Supplemental Information includes seven figures and six tables and can be found with this article online at https://doi.org/10.1016/j.cell.2018.06.035.

ACKNOWLEDGMENTS

We are grateful to the In Vivo Sciences, Molecular Biology, Histology, Imaging, and Neurosurgery & Behavior teams at the Allen Institute for their technical support. We thank Alice Ting for providing the APEX2 construct, Roger Tsien for the tdTomato and ReaChR constructs, Douglas Kim for the GCaMP6f and GCaMP6s constructs, Vincent Pieribone for the ArcLight construct, and Anton Maximov for the DHFR-Cre construct. This work was funded by the Allen Institute for Brain Science, NIH grants MH085500 and DA028298 to H.Z., and NIH grant DA036909 to B.T. M.M.T. and N.M.d.C. are supported by the Intelligence Advanced Research Projects Activity (IARPA) via Department of Interior/Interior Business Center (DoI/IBC) contract number D16PC00004. The U.S. Government is authorized to reproduce and distribute reprints for governmental purposes notwithstanding any copyright annotation thereon. Disclaimer: The views and conclusions contained herein are those of the authors and should not be interpreted as necessarily representing the official policies or endorsements, either expressed or implied, of IARPA, DoI/IBC, or the U.S. Government. The authors wish to thank the Allen Institute founder, Paul G. Allen, for his vision, encouragement, and support.

AUTHOR CONTRIBUTIONS

H.Z., L.M., T.L.D., and B.T. designed the transgenic strategies and provided supervision of the project. L.M., T.L.D., H.G., M.M., and L.A.S. generated all new transgenic mouse lines. R.L. and J.H. provided transgenic colony management. J.P. and K.A.S. managed the genotyping effort. K.A.S., M.J.M., P.R.N., K.E.H., and J.A.H. conducted ISH characterization. T.L.D., L.M., H.G., L.A.S., M.W., E.G., and G.H.L. conducted histological analysis. R.S.L. and J.W. conducted histological analysis in neuromodulatory mice. B.T., L.T.G., Z.Y., O.F., and T.N.N. conducted single-cell RNA-seq study. N.M.d.C. and M.M.T. conducted APEX2 staining and electron microscopy study. T.A.H., A.B.-M., C.A.B., and G.J.M. conducted patch recording and optogenetic study. M.T.V., D.R.O., and J.W. conducted *in vivo* wide-field calcium imaging. L.L., U.K., L.H., and J.L. conducted *in vivo* two-photon calcium imaging. M.Z.L. and M.C. developed and provided ASAP2s and ASAP2s-Kv constructs. E.S.B. developed and provided Chronos and ChrimsonR constructs. J.T.T. developed and provided oChIEF construct. S.M.S. provided project management and coordination with the Jackson Laboratory. H.Z., T.L.D., L.L., T.A.H., M.T.V., N.M.d.C., J.L., and B.T. were main contributors to data analysis and manuscript writing, with inputs from other co-authors.

DECLARATION OF INTERESTS

The authors declare no competing interests.

Received: November 21, 2017
Revised: April 12, 2018
Accepted: June 13, 2018
Published: July 12, 2018

SUPPORTING CITATIONS

The following references appear in the Supplemental Information: Abraira et al. (2017); Bethge et al. (2017); Hsiang et al. (2017); Steinecke et al. (2017); Wang et al. (2017); Zariwala et al. (2012).

REFERENCES

Abraira, V.E., Kuehn, E.D., Chirila, A.M., Springel, M.W., Toliver, A.A., Zimmerman, A.L., Orefice, L.L., Boyle, K.A., Bai, L., Song, B.J., et al. (2017). The cellular and synaptic architecture of the mechanosensory dorsal horn. Cell *168*, 295–310.e219.

Baker, C.A., Elyada, Y.M., Parra, A., and Bolton, M.M. (2016). Cellular resolution circuit mapping with temporal-focused excitation of soma-targeted channelrhodopsin. eLife *5*, e14193.

Bethge, P., Carta, S., Lorenzo, D.A., Egolf, L., Goniotaki, D., Madisen, L., Voigt, F.F., Chen, J.L., Schneider, B., Ohkura, M., et al. (2017). An R-CaMP1.07 reporter mouse for cell-type-specific expression of a sensitive red fluorescent calcium indicator. PLoS ONE *12*, e0179460.

Chamberland, S., Yang, H.H., Pan, M.M., Evans, S.W., Guan, S., Chavarha, M., Yang, Y., Salesse, C., Wu, H., Wu, J.C., et al. (2017). Fast two-photon imaging of subcellular voltage dynamics in neuronal tissue with genetically encoded indicators. eLife *6*, e25690.

Cong, L., Ran, F.A., Cox, D., Lin, S., Barretto, R., Habib, N., Hsu, P.D., Wu, X., Jiang, W., Marraffini, L.A., et al. (2013). Multiplex genome engineering using CRISPR/Cas systems. Science *339*, 819–823.

Dymecki, S.M., Ray, R.S., and Kim, J.C. (2010). Mapping cell fate and function using recombinase-based intersectional strategies. Methods Enzymol. *477*, 183–213.

George, S.H., Gertsenstein, M., Vintersten, K., Korets-Smith, E., Murphy, J., Stevens, M.E., Haigh, J.J., and Nagy, A. (2007). Developmental and adult

phenotyping directly from mutant embryonic stem cells. Proceedings of the National Academy of Sciences of the United States of America *104*, 4455–4460.

Han, H.J., Allen, C.C., Buchovecky, C.M., Yetman, M.J., Born, H.A., Marin, M.A., Rodgers, S.P., Song, B.J., Lu, H.C., Justice, M.J., et al. (2012). Strain background influences neurotoxicity and behavioral abnormalities in mice expressing the tetracycline transactivator. J. Neurosci. *32*, 10574–10586.

Harris, J.A., Hirokawa, K.E., Sorensen, S.A., Gu, H., Mills, M., Ng, L.L., Bohn, P., Mortrud, M., Ouellette, B., Kidney, J., et al. (2014). Anatomical characterization of Cre driver mice for neural circuit mapping and manipulation. Front. Neural Circuits *8*, 76.

Hsiang, J.C., Johnson, K.P., Madisen, L., Zeng, H., and Kerschensteiner, D. (2017). Local processing in neurites of VGluT3-expressing amacrine cells differentially organizes visual information. eLife *6*, e31307.

Huang, Z.J., and Zeng, H. (2013). Genetic approaches to neural circuits in the mouse. Annu. Rev. Neurosci. *36*, 183–215.

Ji, W., Gămănuț, R., Bista, P., D'Souza, R.D., Wang, Q., and Burkhalter, A. (2015). Modularity in the Organization of Mouse Primary Visual Cortex. Neuron *87*, 632–643.

Jin, L., Han, Z., Platisa, J., Wooltorton, J.R., Cohen, L.B., and Pieribone, V.A. (2012). Single action potentials and subthreshold electrical events imaged in neurons with a fluorescent protein voltage probe. Neuron *75*, 779–785.

Klapoetke, N.C., Murata, Y., Kim, S.S., Pulver, S.R., Birdsey-Benson, A., Cho, Y.K., Morimoto, T.K., Chuong, A.S., Carpenter, E.J., Tian, Z., et al. (2014). Independent optical excitation of distinct neural populations. Nat. Methods *11*, 338–346.

Kleinlogel, S., Feldbauer, K., Dempski, R.E., Fotis, H., Wood, P.G., Bamann, C., and Bamberg, E. (2011). Ultra light-sensitive and fast neuronal activation with the Ca^2+-permeable channelrhodopsin CatCh. Nat. Neurosci. *14*, 513–518.

Lam, S.S., Martell, J.D., Kamer, K.J., Deerinck, T.J., Ellisman, M.H., Mootha, V.K., and Ting, A.Y. (2015). Directed evolution of APEX2 for electron microscopy and proximity labeling. Nat. Methods *12*, 51–54.

Li, L., Tasic, B., Micheva, K.D., Ivanov, V.M., Spletter, M.L., Smith, S.J., and Luo, L. (2010). Visualizing the distribution of synapses from individual neurons in the mouse brain. PLoS ONE *5*, e11503.

Lim, S.T., Antonucci, D.E., Scannevin, R.H., and Trimmer, J.S. (2000). A novel targeting signal for proximal clustering of the Kv2.1 K+ channel in hippocampal neurons. Neuron *25*, 385–397.

Lin, J.Y., Knutsen, P.M., Muller, A., Kleinfeld, D., and Tsien, R.Y. (2013). ReaChR: a red-shifted variant of channelrhodopsin enables deep transcranial optogenetic excitation. Nat. Neurosci. *16*, 1499–1508.

Luo, L., Callaway, E.M., and Svoboda, K. (2008). Genetic dissection of neural circuits. Neuron *57*, 634–660.

Madisen, L., Garner, A.R., Shimaoka, D., Chuong, A.S., Klapoetke, N.C., Li, L., van der Bourg, A., Niino, Y., Egolf, L., Monetti, C., et al. (2015). Transgenic mice for intersectional targeting of neural sensors and effectors with high specificity and performance. Neuron *85*, 942–958.

Madisen, L., Mao, T., Koch, H., Zhuo, J.M., Berenyi, A., Fujisawa, S., Hsu, Y.W., Garcia, A.J., 3rd, Gu, X., Zanella, S., et al. (2012). A toolbox of Cre-dependent optogenetic transgenic mice for light-induced activation and silencing. Nat. Neurosci. *15*, 793–802.

Madisen, L., Zwingman, T.A., Sunkin, S.M., Oh, S.W., Zariwala, H.A., Gu, H., Ng, L.L., Palmiter, R.D., Hawrylycz, M.J., Jones, A.R., et al. (2010). A robust and high-throughput Cre reporting and characterization system for the whole mouse brain. Nat. Neurosci. *13*, 133–140.

Oh, S.W., Harris, J.A., Ng, L., Winslow, B., Cain, N., Mihalas, S., Wang, Q., Lau, C., Kuan, L., Henry, A.M., et al. (2014). A mesoscale connectome of the mouse brain. Nature *508*, 207–214.

Ritchie, M.E., Phipson, B., Wu, D., Hu, Y., Law, C.W., Shi, W., and Smyth, G.K. (2015). limma powers differential expression analyses for RNA-sequencing and microarray studies. Nucleic Acids Res. *43*, e47.

Sando, R., 3rd, Baumgaertel, K., Pieraut, S., Torabi-Rander, N., Wandless, T.J., Mayford, M., and Maximov, A. (2013). Inducible control of gene expression with destabilized Cre. Nat. Methods *10*, 1085–1088.

Steinecke, A., Hozhabri, E., Tapanes, S., Ishino, Y., Zeng, H., Kamasawa, N., and Taniguchi, H. (2017). Neocortical chandelier cells developmentally shape axonal arbors through reorganization but establish subcellular synapse specificity without refinement. eNeuro *4*. https://doi.org/10.1523/ENEURO.0057-17.2017.

Steinmetz, N.A., Buetfering, C., Lecoq, J., Lee, C.R., Peters, A.J., Jacobs, E.A.K., Coen, P., Ollerenshaw, D.R., Valley, M.T., de Vries, S.E.J., et al. (2017). Aberrant cortical activity in multiple GCaMP6-expressing transgenic mouse lines. eNeuro *4*. https://doi.org/10.1523/ENEURO.0207-17.2017.

Tasic, B., Menon, V., Nguyen, T.N., Kim, T.K., Jarsky, T., Yao, Z., Levi, B., Gray, L.T., Sorensen, S.A., Dolbeare, T., et al. (2016). Adult mouse cortical cell taxonomy revealed by single cell transcriptomics. Nat. Neurosci. *19*, 335–346.

Ting, J.T., Daigle, T.L., Chen, Q., and Feng, G. (2014). Acute brain slice methods for adult and aging animals: application of targeted patch clamp analysis and optogenetics. Methods Mol Biol. *1183*, 221–242.

Wang, Q., Ng, L., Harris, J.A., Feng, D., Li, Y., Royall, J.J., Oh, S.W., Bernard, A., Sunkin, S.M., Koch, C., and Zeng, H. (2017). Organization of the connections between claustrum and cortex in the mouse. J. Comp. Neurol. *525*, 1317–1346.

Wekselblatt, J.B., Flister, E.D., Piscopo, D.M., and Niell, C.M. (2016). Large-scale imaging of cortical dynamics during sensory perception and behavior. J Neurophysiol *115*, 2852–2866.

Wu, C., Ivanova, E., Zhang, Y., and Pan, Z.H. (2013). rAAV-mediated subcellular targeting of optogenetic tools in retinal ganglion cells in vivo. PLoS ONE *8*, e66332.

Yang, H.H., St-Pierre, F., Sun, X., Ding, X., Lin, M.Z., and Clandinin, T.R. (2016). Subcellular Imaging of Voltage and Calcium Signals Reveals Neural Processing In Vivo. Cell *166*, 245–257.

Zariwala, H.A., Borghuis, B.G., Hoogland, T.M., Madisen, L., Tian, L., De Zeeuw, C.I., Zeng, H., Looger, L.L., Svoboda, K., and Chen, T.W. (2012). A Cre-dependent GCaMP3 reporter mouse for neuronal imaging in vivo. J. Neurosci. *32*, 3131–3141.

Zeng, H., Horie, K., Madisen, L., Pavlova, M.N., Gragerova, G., Rohde, A.D., Schimpf, B.A., Liang, Y., Ojala, E., Kramer, F., et al. (2008). An inducible and reversible mouse genetic rescue system. PLoS Genet. *4*, e1000069.

Zeng, H., and Sanes, J.R. (2017). Neuronal cell-type classification: challenges, opportunities and the path forward. Nat Rev Neurosci *18*, 530–546.

Zhu, P., Aller, M.I., Baron, U., Cambridge, S., Bausen, M., Herb, J., Sawinski, J., Cetin, A., Osten, P., Nelson, M.L., et al. (2007). Silencing and un-silencing of tetracycline-controlled genes in neurons. PLoS ONE *2*, e533.

STAR★METHODS

KEY RESOURCES TABLE

REAGENT or RESOURCE	SOURCE	IDENTIFIER
Antibodies		
Mouse monoclonal anti-parvalbumin antibody	Swant	Cat#PV235; RRID:AB_10000343
Rabbit polyclonal anti-2A peptide antibody	Millipore	Cat#ABS3; RRID:AB_10615498
Mouse monoclonal anti-norepinephrine transporter (NET) antibody	Atlas Antibodies	Cat#AMAb91116; RRID:AB_2665806
Rabbit polyclonal anti-tyrosine hydroxylase (TH) antibody	Abcam	Cat#Ab112; RRID:AB_297840
Mouse monoclonal anti-serotonin transporter (SERT) antibody	Millipore	Cat#MAB1564; RRID:AB_94220
Rabbit polyclonal anti-tryptophan hydroxylase 2 (TPH2) antibody	Millipore	Cat#ABN60; RRID:AB_10806898
Goat polyclonal anti-choline acetyltransferase (ChAT) antibody	Millipore	Cat#AB144P; RRID:AB_262156
Chicken polyclonal anti-GFP antibody	Abcam	Cat#ab13970; RRID:AB_300798
Alexa Fluor 647 donkey anti-mouse IgG	Jackson Immunoresearch	Cat#715-605-151; RRID:AB_2340863
Alexa Fluor 594 donkey anti-rabbit IgG	Jackson Immunoresearch	Cat#711-585-152; RRID:AB_2340621
Alexa Fluor 488 donkey anti-chicken IgG	Jackson Immunoresearch	Cat#703-545-155; RRID:AB_2340375
Bacterial and Virus Strains		
pCAG-FLEX-EGFP-WPRE-pA	UPenn Vector Core	AV-1-ALL854
Chemicals, Peptides, and Recombinant Proteins		
Trimethoprim (TMP)	Sigma-Aldrich	T7883-5G
Tamoxifen (TAM)	Sigma-Aldrich	T5648-5G
Critical Commercial Assays		
SMART-Seq v4	Takara	634888
Deposited Data		
Single cell RNA sequencing data	This paper	GEO: GSE112846
Experimental Models: Cell Lines		
G4 mouse embryonic stem cell line	From the lab of Andras Nagy	George et al., 2007
Ai99 Flp-in mouse embryonic stem cell line	Derived from the G4 line	Madisen et al., 2015
Experimental Models: Organisms/Strains		
Mouse: B6.Cg-Gt(ROSA)$^{26Sortm14(CAG-tdTomato)Hze}$/J, Ai14(RCL-tdT)	The Jackson Laboratory	JAX: 007914
Mouse: B6.129S4-*Gt(ROSA)26Sor*$^{tm3(phiC31*)Sor}$/J, Rosa26-PhiC31	The Jackson Laboratory	JAX: 007743
Mouse: B6;129S-*Gt(ROSA)26Sor*$^{tm65.1(CAG-tdTomato)Hze}$/J, Ai65(RCFL-tdT)	The Jackson Laboratory	JAX: 021875
Mouse: B6.Cg-*Calb1*$^{tm2.1(cre)Hze}$/J, Calb1-IRES2-Cre	The Jackson Laboratory	JAX: 028532
Mouse: B6.Cg-*Calb1*$^{tm1.1(folA/cre)Hze}$/J, Calb1-T2A-dgCre	The Jackson Laboratory	JAX: 023531
Mouse: B6;129S-*Cartpt*$^{tm1.1(cre)Hze}$/J, Cart-IRES2-Cre	The Jackson Laboratory	JAX: 028533

(*Continued on next page*)

Continued

REAGENT or RESOURCE	SOURCE	IDENTIFIER
Mouse: B6;129S-*Esr2*$^{tm1.1(cre)Hze}$/J, Esr2-IRES2-Cre	The Jackson Laboratory	JAX: 030158
Mouse: B6.Cg-*Fezf1*$^{tm1.1(cre/folA)Hze}$/J, Fezf1-T2A-dCre	The Jackson Laboratory	JAX: 025110
Mouse: B6.Cg-*Gnb4*$^{tm1.1(cre/ERT2)Hze}$/J, Gnb4-IRES2-CreERT2	The Jackson Laboratory	JAX: 030159
Mouse: B6;129S-*Htr1a*$^{tm1.1(cre)Hze}$/J, Htr1a-IRES2-Cre	The Jackson Laboratory	JAX: 030160
Mouse: B6;129S-*Npr3*$^{tm1.1(cre)Hze}$/J, Npr3-IRES2-Cre	The Jackson Laboratory	JAX: 031333
Mouse: B6.Cg-*Npy*$^{tm1.1(flpo)Hze}$/J, Npy-IRES2-FlpO	The Jackson Laboratory	JAX: 030211
Mouse: B6;129S-*Oxtr*$^{tm1.1(cre)Hze}$/J, Oxtr-T2A-Cre	The Jackson Laboratory	JAX: 031303
Mouse: B6;129S-*Pdyn*$^{tm1.1(cre/ERT2)Hze}$/J, Pdyn-T2A-CreERT2	The Jackson Laboratory	JAX: 030197
Mouse: B6;129S-*Penk*$^{tm2(cre)Hze}$/J, Penk-IRES2-Cre-neo	The Jackson Laboratory	JAX: 025112
Mouse: Plxnd1-IRES2-dgFlpO	This paper	N/A
Mouse: B6.Cg-*Rasgrf2*$^{tm2.1(folA/flpo)Hze}$/J, Rasgrf2-T2A-dgFlpO	This paper	JAX: 029589
Mouse: B6.Cg-*Rorb*$^{tm3.1(flpo)Hze}$/J, Rorb-IRES2-FlpO	The Jackson Laboratory	JAX: 029590
Mouse: Rorb-P2A-FlpO	This paper	N/A
Mouse: B6;129S-*Slc17a6*$^{tm1.1(flpo)Hze}$/J, Slc17a6-IRES2-FlpO	The Jackson Laboratory	JAX: 030212
Mouse: B6;129S-*Slc17a8*$^{tm1.1(cre)Hze}$/J, Slc17a8-IRES2-Cre	The Jackson Laboratory	JAX: 028534
Mouse: B6.Cg-*Slc32a1*$^{tm1.1(flpo)Hze}$/J, Slc32a1-IRES2-FlpO	The Jackson Laboratory	JAX: 031331
Mouse: B6.Cg-*Slc32a1*$^{tm1.1(flpo)Hze}$/J, Slc32a1-T2A-FlpO	The Jackson Laboratory	JAX: 029591
Mouse: Tacr1-T2A-Cre	This paper	N/A
Mouse: Tnnt1-IRES2-CreERT2	This paper	N/A
Mouse: B6;129S-*Vipr2*$^{tm1.1(cre)Hze}$/J, Vipr2-IRES2-Cre	The Jackson Laboratory	JAX: 031332
Mouse: Ai31(RCL-Syp-EmGFP)	This paper	N/A
Mouse: B6;129S-*Gt(ROSA)26Sor*$^{tm34.1(CAG-Syp/tdTomato)Hze}$/J, Ai34(RCL-Syp-tdT)	The Jackson Laboratory	JAX: 012570
Mouse: B6.Cg-*Gt(ROSA)26Sor*$^{tm40.1(CAG-aop3/EGFP)Hze}$/J, Ai40(RCL-ArchT-EGFP)	The Jackson Laboratory	JAX: 021188
Mouse: Ai47(RCL-triGFP)	This paper	N/A
Mouse: Ai63(TIT-tdT)	This paper	N/A
Mouse: Ai65F(RCF-tdT)	This paper	N/A
Mouse: Ai66R(RCR-tdT)	This paper	N/A
Mouse: B6.Cg-*Gt(ROSA)26Sor*$^{tm75.1(CAG-tdTomato*)Hze}$/J, Ai75(RCL-nT)	The Jackson Laboratory	JAX: 025106
Mouse: B6.Cg-*Gt(ROSA)26Sor*$^{tm80.1(CAG-COP4*L132C/EYFP)Hze}$/J, Ai80(RCFL-CatCh)	The Jackson Laboratory	JAX: 025109
Mouse: Ai86(TITL-ArcLight)	This paper	N/A
Mouse: B6.Cg-*Igs7*$^{tm90.1(tetO-COP4*/EGFP)Hze}$/J, Ai90(TITL-Chronos)	The Jackson Laboratory	JAX: 024100

(*Continued on next page*)

Continued

REAGENT or RESOURCE	SOURCE	IDENTIFIER
Mouse: Ai110(RCL-FnGF-nT)	This paper	N/A
Mouse: B6.Cg-*Igs7*$^{tm133.1(tetO\text{-}apx1*)Hze}$/J, Ai133(TITL-ssAPEX2tm)	The Jackson Laboratory	JAX: 030213
Mouse: B6.Cg-*Igs7*$^{tm134.1(tetO\text{-}ChR2\text{-}EYFP)Hze}$/J, Ai134(TITL-ChR2-YFP)	The Jackson Laboratory	JAX: 031334
Mouse: B6.Cg-*Igs7*$^{tm136.1(tetO\text{-}COP3*/COP4*/EYFP)Hze}$/J, Ai136(TITL-ReaChR-YFP)	The Jackson Laboratory	JAX: 030216
Mouse: B6.Cg-*Igs7*$^{tm139.1(tetO\text{-}EGFP,CAG\text{-}tdTomato,\text{-}tTA2)Hze}$/J, Ai139(TIT2L-GFP-ICL-TPT)	The Jackson Laboratory	JAX: 030219
Mouse: B6.Cg-*Igs7*$^{tm140.1(tetO\text{-}EGFP,CAG\text{-}tTA2)Hze}$/J, Ai140(TIT2L-GFP-ICL-tTA2)	The Jackson Laboratory	JAX: 030220
Mouse: B6.Cg-*Igs7*$^{tm148.1(tetO\text{-}GCaMP6f,CAG\text{-}tTA2)Hze}$/J, Ai148(TIT2L-GC6f-ICL-tTA2)	The Jackson Laboratory	JAX: 030328
Mouse: B6.Cg-*Igs7*$^{tm161(tetO\text{-}GFP,CAG\text{-}tTA2)Hze}$/J, Ai161(TIT2L-GFP-ICR-tTA2)	The Jackson Laboratory	JAX: 031561
Mouse: B6.Cg-*Igs7*$^{tm162(tetO\text{-}GCaMP6s,CAG\text{-}tTA2)Hze}$/J, Ai162(TIT2L-GC6s-ICL-tTA2)	The Jackson Laboratory	JAX: 031562
Mouse: Ai163(TIT2L-GC6s-ICL-TPT)	This paper	N/A
Mouse: Ai167(TIT2L-ChrimsonR-tdT-ICL-tTA2)	This paper	N/A
Mouse: Ai168(TIT2L-oChIEF-P2A-tdT-ICL-tTA2)	This paper	N/A
Mouse: B6.Cg-*Igs7*$^{tm169(tetO\text{-}ASAP2s,CAG\text{-}tTA2)Hze}$/J, Ai169(TIT2L-ASAP2s-ICL-tTA2)	The Jackson Laboratory	JAX: 031569
Mouse: B6.Cg-*Igs7*$^{tm170(tetO\text{-}ASAP2s\text{-}Kv,CAG\text{-}tTA2)Hze}$/J, Ai170(TIT2L-ASAP2s-Kv-ICL-tTA2)	The Jackson Laboratory	JAX: 031570
Mouse: B6.Cg-*Chrm2*$^{tm1.1Hze}$/J, Chrm2-tdT	The Jackson Laboratory	JAX: 030330
Recombinant DNA		
pX330-U6-Chimeric_BB-CBh-hSpCas9	Cong et al., 2013	Addgene Cat# 42230
pCAG-FlpE	Open Biosystems	No longer available
Ai62(TITL-tdT) Flp-in replacement vector	Madisen et al., 2015	Addgene Cat# 61576
Calb1-IRES2-Cre targeting vector	This paper	N/A
Calb1-T2A-dgCre targeting vector	This paper	N/A
Cart-IRES2-Cre targeting vector	This paper	N/A
Esr2-IRES2-Cre donor and guide vectors	This paper	N/A
Fezf1-T2A-dCre targeting vector	This paper	N/A
Gnb4-IRES2-CreERT2 targeting vector	This paper	N/A
Htr1a-IRES2-Cre donor and guide vectors	This paper	N/A
Npr3-IRES2-Cre targeting vector	This paper	N/A
Npy-IRES2-FlpO donor and guide vectors	This paper	N/A
Oxtr-T2A-Cre donor and guide vectors	This paper	N/A
Pdyn-T2A-CreERT2 donor and guide vectors	This paper	N/A
Penk-IRES2-Cre-neo targeting vector	This paper	N/A
Plxnd1-IRES2-dgFlpO targeting vector	This paper	N/A
Rasgrf2-T2A-dgFlpO targeting vector	This paper	N/A
Rorb-IRES2-FlpO targeting vector	This paper	N/A
Rorb-P2A-FlpO targeting vector	This paper	N/A
Slc17a6-IRES2-FlpO donor and guide vectors	This paper	N/A
Slc17a8-IRES2-Cre donor and guide vectors	This paper	N/A
Slc32a1-IRES2-FlpO targeting vector	This paper	N/A
Slc32a1-T2A-FlpO targeting vector	This paper	N/A

(*Continued on next page*)

Continued

REAGENT or RESOURCE	SOURCE	IDENTIFIER
Tacr1-T2A-Cre targeting vector	This paper	N/A
Tnnt1-IRES2-CreERT2 targeting vector	This paper	N/A
Vipr2-IRES2-Cre donor and guide vectors	This paper	N/A
Ai31(RCL-Syp-EmGFP) targeting vector	This paper	N/A
Ai34(RCL-Syp-tdT) targeting vector	This paper	N/A
Ai40(RCL-ArchT-EGFP) targeting vector	This paper	N/A
Ai47(RCL-triGFP) targeting vector	This paper	N/A
Ai63(TI-TRE-tdT) Flp-in targeting vector	This paper	N/A
Ai65F(RCF-tdT) targeting vector	This paper	N/A
Ai66R(RCR-tdT) targeting vector	This paper	N/A
Ai75(RCL-nT) targeting vector	This paper	N/A
Ai80(RCFL-CatCh) targeting vector	This paper	N/A
Ai86(TITL-ArcLight) Flp-in targeting vector	This paper	N/A
Ai90(TITL-Chronos) Flp-in targeting vector	This paper	N/A
Ai110(RCL-FnGF-nT) targeting vector	This paper	N/A
Ai133(TITL-ssAPEX2tm) Flp-in targeting vector	This paper	N/A
Ai134(TITL-ChR2-YFP) Flp-in targeting vector	This paper	N/A
Ai136(TITL-ReaChR-YFP) Flp-in targeting vector	This paper	N/A
Ai139(TIT2L-GFP-ICL-TPT) Flp-in targeting vector	This paper	N/A
Ai140(TIT2L-GFP-ICL-tTA2) Flp-in targeting vector	This paper	N/A
Ai148(TIT2L-GC6f-ICL-tTA2) Flp-in targeting vector	This paper	N/A
Ai161(TIT2L-GFP-ICR-tTA2) Flp-in targeting vector	This paper	N/A
Ai162(TIT2L-GC6s-ICL-tTA2) Flp-in targeting vector	This paper	N/A
Ai163(TIT2L-GC6s-ICL-TPT) Flp-in targeting vector	This paper	N/A
Ai167(TIT2L-ChrimsonR-tdT-ICL-tTA2) Flp-in targeting vector	This paper	N/A
Ai168(TIT2L-oChIEF-P2A-tdT-ICL-tTA2) Flp-in targeting vector	This paper	N/A
Ai169(TIT2L-ASAP2s-ICL-tTA2) Flp-in targeting vector	This paper	N/A
Ai170(TIT2L-ASAP2s-Kv-ICL-tTA2) Flp-in targeting vector	This paper	N/A
Chrm2-tdT donor and guide vectors	This paper	N/A
Software and Algorithms		
GraphPad Prism software, version 7.0	GraphPad	https://www.graphpad.com/scientific-software/prism/
ImageJ	National Institutes of Health	https://imagej.nih.gov/ij/download.html
Fiji software	GPL v2, Fiji	http://fiji.sc/Fiji
STAR v2.5.3	Github	https://github.com/alexdobin/STAR
MATLAB 9.1 (R2016b)	Mathworks	https://www.mathworks.com/
Python 2.7	Python	https://www.python.org/downloads/
Igor Pro	Wavemetrics	https://www.wavemetrics.com/

CONTACT FOR REAGENT AND RESOURCE SHARING

Further information and requests for resources and reagents should be directed to and will be fulfilled by the Lead Contact, Hongkui Zeng (hongkuiz@alleninstitute.org).

EXPERIMENTAL MODEL AND SUBJECT DETAILS

Animal care and use

Both male and female transgenic mice $\geq$ P56 were utilized for all experiments. All animals were housed 3-5 per cage and maintained on a 12-hour light/dark cycle, in a humidity- and temperature-controlled room with water and food available *ad libitum*. All

experimental procedures related to the use of mice were conducted with approved protocols in accordance with NIH guidelines, and were approved by the Institutional Animal Care and Use Committee (IACUC) of the Allen Institute for Brain Science.

METHOD DETAILS

Transgenic mice generation

All targeting vectors were constructed using gene synthesis and standard molecular cloning approaches. Knock-in driver line and Rosa26-based reporter vectors contained components that were previously described (Madisen et al., 2015; Madisen et al., 2010). For TIGRE1.0- and 2.0- based reporters, vectors containing the following components were constructed: FRT3 – 2X HS4 chicken beta globin insulators – TRE_{tight} (1.0 lines) or TRE2 (2.0 lines) promoter – LoxP – ORF-3X stops – hGH poly(A), PGK polyA) – LoxP – gene – WPRE- bGH poly(A) – 2X HS4 chicken beta globin insulators – CAG promoter – Lox2272 – ORF-3X stops – hGH poly(A), TK poly(A) – Lox2272 – tTA2 – WPRE – bGH poly(A) – Hygro-SD – FRT5. Targeting of the transgene cassettes into an endogenous gene locus or the Rosa26 locus was accomplished via standard homologous recombination using linearized targeting vector DNA or via CRISPR/Cas9-mediated genome editing using circularized targeting vector in combination with a gene-specific guide vector (Addgene plasmid #42230). Targeting of the transgene cassettes into the TIGRE locus was accomplished via Flp-recombinase mediated cassette exchange (RMCE) using circularized targeting vector and a CAG-FlpE vector (Open Biosystems) as previously described (Madisen et al., 2015). The129S6B6F1 ES cell line, G4, was utilized directly for driver line and Rosa26-based reporter line targeting. A Flp-recombinase landing pad ES cell line derived from G4 cells that was previously described (Madisen et al., 2015) was utilized for RMCE into the TIGRE locus. Correctly targeted ES cells were identified using standard screening approaches (PCR, qPCR, and Southern blots) and injected into blastocysts to obtain chimeras and subsequent germline transmission. Resulting mice were crossed to the Rosa26-PhiC31 mice (JAX Stock # 007743) to delete the pPGK-neo or pPGK-hygro selection marker cassette, and then backcrossed to C57BL/6J mice and maintained in C57BL/6J congenic background. TIGRE2.0 reporter lines Ai139, Ai140 and Ai148 have been bred to homozygosity and are maintained in this state without any notable issues. Only mice heterozygous for both reporter and driver transgenes were used for experiments.

Administration of trimethoprim or tamoxifen

Induction of DHFR-domain containing dCre, dgCre or dgFlpO driver lines was done by administration via oral gavage (PO) of trimethoprim (TMP) at 0.3 mg/g body weight per day for 3 days in an adult mouse. TMP working solution was diluted from a 10x stock in 100% DMSO with a 2% methylcellulose solution. The GFP part present in dgCre and dgFlpO lines exhibits no visible fluorescence with or without TMP induction. Induction of CreERT2 driver lines was done by administration via oral gavage (PO) of tamoxifen (50 mg/ml in corn oil) at 0.2 mg/g body weight per day for 1-5 days in an adult mouse, or 1 day in a mouse younger than P28. Mice can be used for experiments starting at 1-2 weeks after TMP or tamoxifen dosing.

In situ hybridization

All *in situ* hybridization (ISH) was performed via a standardized production platform that was previously described (Harris et al., 2014; Madisen et al., 2010). Data can be found in the AIBS Transgenic Characterization database (http://connectivity.brain-map.org/transgenic/search/basic).

Brain region acronyms: ARH, arcuate hypothalamic nucleus. CEA, central amygdalar nucleus. CLA, claustrum. CP, caudoputamen. CTX, cortex. DR, dorsal nucleus raphe. ENTl, entorhinal area, lateral part. ENTm, entorhinal area, medial part. EW, Edinger-Westphal nucleus. HPF, hippocampal formation. LC, locus ceruleus. LGd, dorsal part of the lateral geniculate complex. LGv, ventral part of the lateral geniculate complex. MEA, medial amygdalar nucleus. SI, substantia innominate. SNc, substantia nigra, compact part. TH, thalamus. VMH, ventromedial hypothalamic nucleus. VPM, ventral posteromedial nucleus of the thalamus.

Immunohistochemistry and imaging

Mice were transcardially perfused with 0.1M phosphate buffered saline (PBS) followed by 4% paraformaldehyde (PFA). Brains were removed, post-fixed in PFA overnight, followed by an additional incubation overnight in 30% sucrose. Coronal or sagittal sections (50 μm) were cut using a freezing microtome and sections were stored in PBS until use. For parvalbumin or 2A antibody staining, free floating brain sections were rinsed three times in phosphate-buffered saline (PBS), blocked for 1 hour in PBS containing 5% donor donkey serum, 2% bovine serum albumin (BSA) and 0.1% Triton X-100, and incubated overnight at 4°C in the anti-parvalbumin primary antibody (PV, 1:3000, Swant PV235) or in the anti-2A peptide primary antibody (2A, 1:500, Millipore ABS31). The following day, sections were washed three times in PBS, followed by incubation in blocking solution containing an Alexa 647 conjugated secondary antibody (1:250, Jackson 715-605-151), washed in PBS, and mounted in Vectashield containing DAPI (H-1500, Vector Labs). For all other antibody staining, sections were subjected to antigen retrieval with 10 mM sodium citrate pH 6.0 with 0.05% Triton X-100 (heated to 75°C for 20 minutes), rinsed, and then blocked with 5% normal donkey serum and 0.2% Triton X-100 in PBS for one hour. Tissue was then incubated in primary antibodies diluted in the blocking solution for 48-72 hours at 4°C, washed the following day in 0.2% Triton X-100 in PBS and then incubated in the appropriate Alexa-conjugated secondary antibodies (1:500, ThermoFisher). Sections were then rinsed in 0.2% Triton X-100 in PBS, followed by PBS alone, mounted on gelatin-coated slides and coverslipped with prolong diamond antifade mounting media (P36965, ThermoFisher). The following primary antibodies were used to detect transgene

expression in neuromodulatory cell types: anti-norepinephrine transporter (NET, 1:500, Atlas Antibodies AMAb91116), anti-tyrosine hydroxylase (TH, 1:1000, Abcam ab112), anti-serotonin transporter (SERT, 1:500, EMDMillipore MAB1564), anti-tryptophan hydroxylase 2 (TPH2, 1:250, EMDMillipore ABN60), anti-choline acetyltransferase (ChAT, 1:300, EMDMillipore AB144P). In a subset of experiments, we compared antibody-enhancement to native GCaMP6 fluorescence using an anti-GFP primary antibody (1:5000, Abcam, Ab13970) and donkey anti-chicken secondary antibody (703-545-155, Jackson ImmunoResearch). Images (1024 X 1024) of native or antibody-enhanced fluorescence were collected on a TissueCyte 1000 (Tissue Vision), an Olympus Fluoview FV1000 confocal microscope or a Leica SP8 resonant-scanning confocal microscope and were manually counted for each experimental condition using the cell counter plugin within ImageJ (K. De Vos, University of Sheffield) by observers blind to the genotype of the animals.

Electron Microscopy

Mice were transcardially perfused with a fixative mixture of 2.5% paraformaldehyde and 1.25% glutaraldehyde. After dissection, coronal slices were cut with a vibratome and post-fixed for 12 – 48 h. To visualize APEX2, slices were incubated in a solution of 3,3′-diaminobenzidine (0.3 mg/mL, or 1.4 mM), 2.5 mM ammonium nickel sulfate, in 0.1 M phosphate buffer. Following incubation, hydrogen peroxide was added to a final concentration of 1 mM and the DAB reaction was monitored under a dissecting microscope. After sufficient reaction time, sections were extensively washed and prepared for reduced osmium treatment (rOTO). Ferricyanide was used to reduce Osmium and Thiocarbohydrazide (TCH) for further intensification of the staining. Uranyl acetate and lead aspartate were used to enhance contrast. After resin embedding, ultrathin sections (40 nm) were cut in a Leica ultra-microtome and imaged with Transmission electron microscopy in a JEOL 1200 EX II.

Single-cell RNA-sequencing

For comparison of reporter transgene expression level, we injected AAV2/1-pCAG-FLEX-EGFP-WPRE-pA (Oh et al., 2014) into VISp of two male Snap25-IRES2-Cre mice at P25 and P44 respectively. Stereotaxic injection procedures were performed as previous described (Oh et al., 2014). The mouse injected at P25 was allowed to survive for 32 days post injection, and cells were collected when the mouse was P57. The mouse injected at P44 was allowed to survive for 21 days post injection, and cells were collected when the mouse was P65. We collected GFP-positive cells from L1-3, L4, L5, and L6 at the injection site.

Cells from transgenic mice or transgenic mice injected with AAV-pCAG-FLEX-EGFP-WPRE-pA were collected by microdissection, single-cell suspension, and single-cell FACS. All cells were FACS-isolated with selection for one of the fluorescent proteins: green fluorescence for Pvalb-T2A-CreERT2;Ai139, Pvalb-IRES-Cre;Ai162, Pvalb-IRES-Cre;Ai163, Sst-IRES-Cre;Ai14;Ai148, and Scnn1a-Tg3-Cre;Ai139; red fluorescence for Pvalb-IRES-Cre;Ai14, Sst-IRES-Cre;Ai14, Rbp4-Cre_KL100;Ai14, Rbp4-Cre_KL100;Ai14;Ai148, Scnn1a-Tg3-Cre;Ai14 and Snap25-IRES2-Cre;Ai14 cells.

Cells were then frozen at −80°C, and were later processed for scRNA-seq using the SMART-Seq v4 method, as described in the Allen Institute Transcriptomics Technical Whitepaper (http://help.brain-map.org/download/attachments/8323525/CellTypes_Transcriptomics_Overview.pdf) (Tasic et al., 2016). After sequencing, raw data was quantified using STAR v2.5.3 and were aligned to both a Ref-Seq transcriptome index for the mm10 genome, and a custom index consisting of transgene sequences. FPKM values were calculated by dividing raw counts for each transgene by the length of each gene in kilobases and by the total number of reads that mapped to both the transcripome index and to the transgene sequences in millions of reads.

To examine transcriptome-wide gene expression changes, scRNA-seq datasets were mapped to reference transcriptomic cell types using nearest centroid classifiers. Differentially expressed genes between groups of cells were detected using limma voom mode (Ritchie et al., 2015).

In vivo two-photon calcium imaging in cortical interneurons

Detailed surgical and imaging procedures have been published previously (Madisen et al., 2015). Briefly, adult mice (2-5 months old, both genders, n = 13, including 2 Sst-IRES-Cre;Ai14;Ai95, 2 Sst-IRES-Cre;Ai14;Ai148, 3 Pvalb-IRES-Cre; Ai163, 1 Pvalb-IRES-Cre; Ai162, 2 Pvalb-IRES-Cre;Ai14;Ai148 and 3 Vip-IRES-Cre;Ai14;Ai148 mice) were implanted with a metal head-post and a 3-5-mm cranial window over the left visual cortical area under anesthesia. After 7 days of recovery from surgery, mice were habituated to head fixation and presentation of visual stimulations on an in-house made running device (a freely-rotating running disc) for 2 weeks before imaging experiment started. During imaging, mice were awake, head-fixed but allowed to run or rest on the freely-rotating running disc with or without visual stimuli presented on a calibrated LCD monitor spanning 60° in elevation and 130° in azimuth to the contralateral (right) eye. For visually evoked responses, whole-screen sinusoidal drifting gratings were presented showing 8 orientations (0° to 315° in 45° increment), 3 or 4 spatial frequencies (SFs, [0.02, 0.04, 0.08] or [0.02, 0.04, 0.08 and 0.16] cycle per degree) and 1 temporal frequency (2 Hz), presented at 80% contrast in a random sequence for 8 repetitions. Each drifting grating lasted for 2 s with an interstimulus-interval of 1 or 2 s. A gray screen at mean illuminance was presented randomly for 16 times. The mouse's eye was positioned ~22 cm away from the center of the monitor. Due to the choice of whole-screen visual stimuli, we did not track the eye position.

Two-photon calcium imaging was performed using a Bruker (Prairie) two-photon microscope with 8 kHz resonant scanners, coupled with a Chameleon Ultra II Ti:sapphire laser system (Coherent). In the current study, we crossed the Ai148 reporter lines with Pvalb-, Sst- and Vip-IRES-Cre;Ai14 mice to co-express the GECI GCaMP6f together with a red, calcium insensitive cytosol marker tdTomato in PV, SST and VIP positive inhibitory interneurons, respectively. Co-expression of tdTomato facilitated locating

and calcium imaging those interneurons with low expression of GECI. Fluorescence excited at 920 nm wavelength with < 70 mW laser power measured after objective was collected in two spectral channels using green (510/42 nm) and red (641/75 nm) emission filters. The emission filter set we selected ensured good separation between red and green channels. Fluorescence images were acquired at various frame rates (512X512 pixels, 30 Hz; 256X256 pixels, 60 Hz) through a 16x water-immersion objective lens (Nikon, NA 0.8), with or without visual stimulations.

In vivo two-photon calcium imaging in cortical excitatory neurons

Imaging of the Ai93 and Ai148 reporter lines crossed with Ntsr1-Cre_GN220 and Tlx3-Cre_PL56, which express GCaMP6f in deep cortical layer 6 and 5 respectively, was conducted in the Allen Brain Observatory pipeline. Briefly, adult mice (from P37 to P63, both sexes, n = 7) were implanted with a metal head-post and a ~5-mm cranial window over the left visual cortical area under anesthesia. After 7 days of recovery from surgery, the visual cortex was mapped using intrinsic imaging. An automated segmentation and annotation module was developed to delineate boundaries between visual areas. To provide a reliable targeting of two-photon calcium imaging experiments, a consistent anatomical coordinate corresponding to the center of V1 (which maps to center of the retina) was used.

Mice were then habituated to head fixation and presentation of visual stimulations on an in-house made running device (a freely-rotating running disc) for 2 weeks before imaging experiment started. During imaging, mice were awake, head-fixed but allowed to run or rest on the freely-rotating running disc with or without visual stimuli presented on a calibrated LCD monitor.

The screen spanned 120° X 95° of visual space and was positioned 15 cm from the mouse (118.6 mm lateral, 86.2 mm anterior and 31.6 mm dorsal to the right eye). Each screen (ASUS PA248Q LCD monitor) was gamma calibrated using a USB-650 Red Tide Spectrometer (Ocean Optics). Luminance was measured using a SpectroCAL MKII Spectro radiometer (Cambridge Research Systems). Monitors brightness (30%) and contrast (50%) corresponded to a mean luminance of 50 cd/m2.

For quantifying grating responses, the stimulus consisted of a full field drifting sinusoidal grating at a single spatial frequency (0.04 cycles/degree) and contrast (80%). The grating was presented at 8 different directions (separated by 45°) and at 5 temporal frequencies (1, 2, 4, 8, 15 Hz). Each grating was presented for 2 s, followed by 1 s of mean luminance gray before the next grating. Each grating condition (direction & temporal frequency combination) was presented 15 times, in a random order. There were blank sweeps (i.e., mean luminance gray instead of grating) presented approximately once every 20 gratings.

Two-photon calcium imaging was performed using a Nikon A1R MP+. The Nikon system was adapted to provide space to accommodate the behavior apparatus. Laser excitation was provided by a Ti:Sapphire laser (Chameleon Vision – Coherent) at 910 nm. Pre-compensation was set at ~10,000 fs2. Movies were recorded at 30Hz using resonant scanners over a 400-μm field of view. Two-photon movies (512x512 pixels, 30Hz), eye tracking (30Hz), and behavior (30Hz) were recorded and continuously monitored. We imaged the deep cortical layers (layer 5 and 6) through a 16x water-immersion objective lens (Nikon, NA 0.8) using less than 240 mW (measured after objective) to avoid brain damage.

Acute slice physiology and optogenetics

Para-sagittal slices were prepared from 6-16 weeks old mice of either sex. Mice were anaesthetized with isoflurane, decapitated and brains were swiftly removed. 350 μm slices were cut using a Leica VT1200S vibratome in ice cold slicing solution. Slicing solution contained 87 mM NMDG, 2.5 mM KCl, 1.2 mM NaH_2PO_4, 30 mM $NaHCO_3$, 20 mM HEPES, 25 mM glucose, 12 mM N-acetyl cysteine, 5 mM Na-ascorbate, 2 mM thiourea, 3 mM Na-pyruvate, 10 mM $MgSO_4$, 0.5 mM $CaCl_2$. pH was adjusted to 7.3-7.4 using HCl. Slices were stored in slicing solution for 15 minutes at 34°C, after which they were transferred to artificial cerebrospinal fluid (ACSF) and stored at room temperature until use. ACSF contained 124 mM NaCl, 2.5 mM KCl, 1.2 mM NaH_2PO_4, 24 mM $NaHCO_3$, 5 mM HEPES, 12.5 mM glucose, 2 mM $MgSO_4$ and 2 mM $CaCl_2$. pH was adjusted to 7.3-7.4 mM using NaOH, osmolarity = 290-300 mOsm. Prior to use, slices were transferred to a recording chamber continuously perfused with ACSF heated to 32 ± 2°C. Recordings were made using 3 – 5 MΩ borosilicate glass pipettes. Internal solution contained 130 mM K-gluconate, 4 mM KCl, 10 mM HEPES, 0.3 mM EGTA, 10 mM phosphocreatine disodium salt, 4 mM MgATP and 0.3 mM Na-GTP. During recording, 10 μM NBQX was added to ACSF to block excitatory synaptic transmission. Measurements of photocurrents were performed with neurons clamped to −70 mV. 100 nM tetrodotoxin was added to the bath to block voltage-gated sodium channels in voltage clamp recordings. Access resistance was < 20 MΩ at the start of all experiments and was monitored throughout the experiment. Recordings were terminated if access resistance increased to > 25 MΩ. Data were recorded using Multiclamp 700B amplifiers (Axon Instruments) and digitized using ITC-18 data acquisition interfaces (Heka). Data were acquired using custom scripts in Igor Pro (Wavemetrics).

Photostimulation of cells was performed using either a 470 nm or 590 nm LED reflected into a 63x/1.0 NA water immersion objective. The power of the light stimulus was controlled via pulse-width modulation of TTL signals passed to an analog LED driver (LightSpeed Technologies). Powers were measured using a power meter (Thor Labs PM-100A) placed after the objective. Experiments measuring action potential (AP) entrainment at different frequencies utilized different pulse widths for each transgenic line. This was to accommodate the differences in minimum light duration necessary to evoke a single AP (Figure S6F). Pulse durations utilized were Ai90: 1 ms; Ai134: 0.5 ms, Ai136: 0.05 ms, and Ai167: 0.2 ms. Experiments performed using longer pulses in Ai136 and Ai167 mice generally resulted in multiple APs in response to the first pulse, followed by decreased fidelity at the end of the pulse train.

Wide-field calcium imaging

Wide-field calcium imaging was performed either through the intact skull or through a 5-mm-diameter chronically implanted cranial window centered over the left visual cortex. For through-skull imaging, the skull was exposed and cleared of periosteum, and a #1.5 borosilicate coverslip (Electron Microscopy Sciences, #72204-01) was fixed to the skull surface by a layer of clear cement (C&B Metabond, Sun Medical Co.). A 3D-printed light shield was fixed around the coverslip using additional Metabond, and the outward-facing surfaces were coated with an opaque resin (Lang Dental Jetliquid, MediMark). Mice with chronically implanted windows received a 5-mm-diameter craniotomy over the left hemisphere, centered at 2.7 mm lateral and 1.3 mm anterior to lambda. The craniotomy was sealed with a stack of three #1 coverslips, attached to each other using optical adhesive (Norland) and to the skull with Metabond. The window provided optical access to the left visual cortex, the posterior aspect of somatosensory cortex and medial aspect of dorsal retrosplenial cortex. In both cases, a custom-manufactured titanium headpost was fixed posterior to the lightshield/coverslip and dorsal to the cerebellum using Metabond. All surgical procedures were performed under isoflurane anesthesia. Image acquisition used a Hamamatsu Flash4.0 v2 or v3 sCMOS camera running with a 10-ms rolling exposure (100 Hz). Images were produced by a tandem-lens macroscope (Scimedia THT-FLSP) with 1.0x tube and objective lenses (Leica 10450028) for through skull imaging or a 1.0x tube lens paired to a 1.6x objective lens (Leica 10450029) for imaging through the chronically implanted window. Epifluorescence illumination used a 470-nm LED (Thorlabs M470L3) filtered (Semrock FF01-474/27-50) and reflected by a dichroic mirror (Semrock FF495-Di03-50 x70) through the objective lens. Fluorescence emission passed through a filter (Semrock FF01-525/45-50) to the camera. At all locations, mice were either male or female and were 7–30 weeks of age.

QUANTIFICATION AND STATISTICAL ANALYSIS

Transgene expression data were analyzed and graphed using GraphPad Prism 7.02 software (Hearne Scientific Software, Chicago, IL). Data presented are mean ± standard error from the mean.

In vivo two-photon calcium imaging data collected from cortical interneurons were analyzed with in-house developed MATLAB scripts. In summary, data were corrected for in-plane motion artifacts using cross-correlation motion correction method between frames. Image segmentation was done using Independent Component Analysis (ICA) followed by automated Region of Interest (ROI) selection with manual confirmation/correction. Green fluorescence signal of all pixels within each ROI was averaged by image frames. Fluorescence signal from the red channel was not quantitatively analyzed. No neuropil signal subtraction was done for these data. The baseline for $\Delta F/F$ calculation was determined from the mean fluorescence within a 0.5 s window prior to visual stimulus onset.

In vivo two photon calcium imaging data collected from cortical excitatory neurons were analyzed with in-house developed scripts. A comprehensive description of the data analysis pipeline is available on the Allen Brain Observatory portal (http://help.brain-map.org/display/observatory/Documentation). Briefly, each pixel of the calcium movie was first corrected for pixel leakage, then each frame was motion corrected to a reference frame. A rule-based segmentation algorithm automatically extracted all ROIs covering active somatic compartments. For each ROI, neuropil signals were then subtracted and nearby ROIs were unmixed. Each ROI associated trace was then converted to $\Delta F/F$. For drifting grating quantification, tuning was calculated from the averaged response over the duration of stimulus presentation.

Analysis of acute physiology and optogenetics data was performed using Igor Pro and custom Python (2.7) scripts combined with the Allen Institute Software Development Kit to measure the timing of APs in whole cell recordings. Statistical comparisons of population averages of transgenic lines were made by first performing a one-way ANOVA, followed by unpaired t tests between groups with a Bonferroni correction for multiple comparisons (either 6 comparisons between 4 groups, $\alpha = 0.0083$; or 10 comparisons between 5 groups, $\alpha = 0.005$). Throughout the study, sample number n = number of cells recorded.

Wide-field calcium imaging data were spatially downsampled by averaging, and calcium traces were obtained by subtracting and then dividing each pixel by its mean over the entire time series. Traces were analyzed by finding peaks and computing two parameters: prominence and full-width at half-prominence. Prominence is defined as the height of the peak relative to the greater of the two minima between the peak and its surrounding two higher peaks (or beginning/end of trace if no higher peak). Peak detection used PeakUtils 1.0.3 (Python 2.7).

DATA AND SOFTWARE AVAILABILITY

The accession number for the single-cell RNA-sequencing data reported in this paper is GEO: GSE112846.

Supplemental Figures

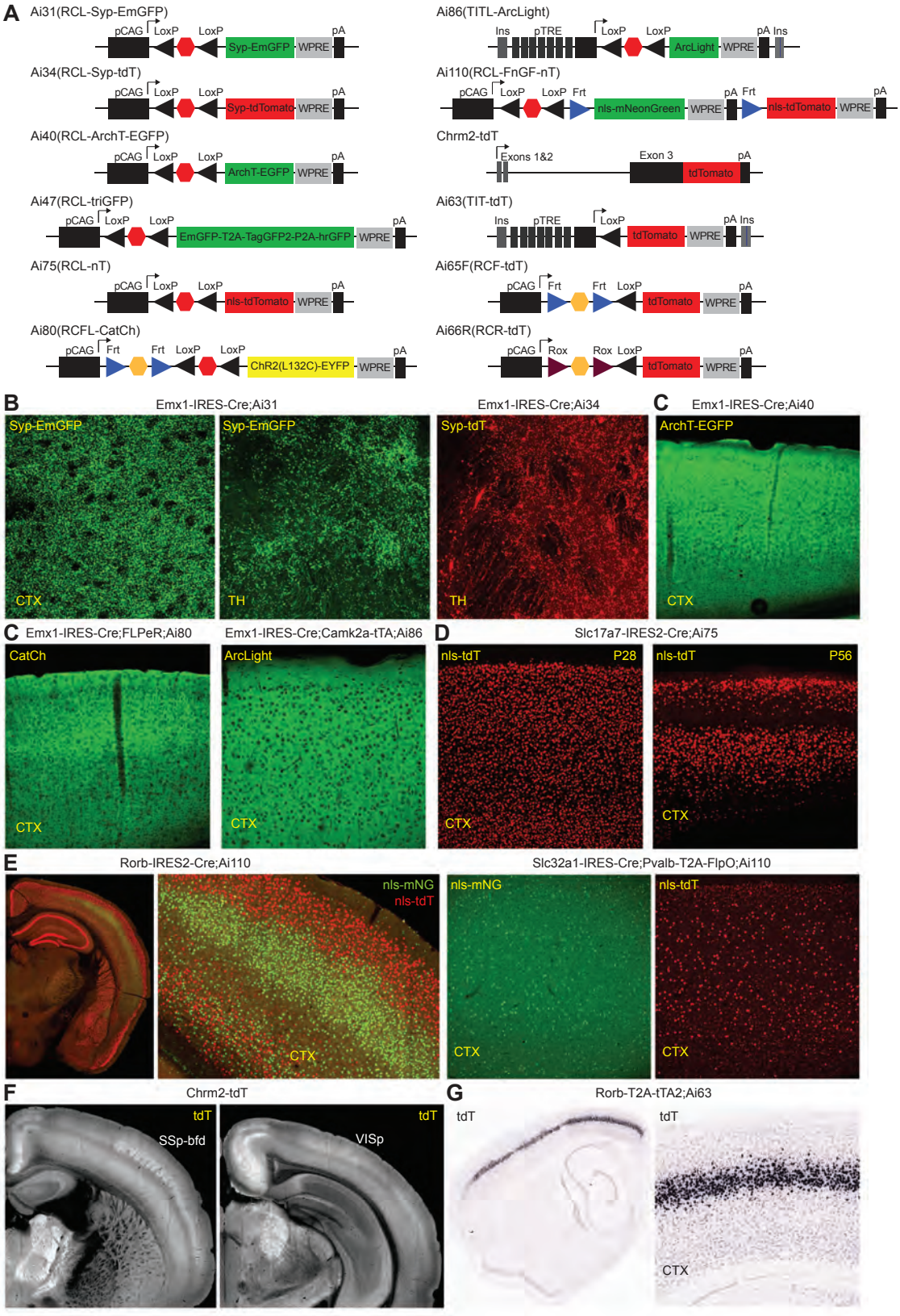

(legend on next page)

Figure S1. Expression Validation of New Transgenic Reporter Lines, Related to Figure 2

(A) Schematic diagrams of new transgenic reporter lines. RCL, Rosa26 – CAG promoter – LoxP-STOP-LoxP. RCFL, Rosa26 – CAG promoter – FRT-STOP-FRT – LoxP-STOP-LoxP. RCF, Rosa26 – CAG promoter – FRT-STOP-FRT. RCR, Rosa26 – CAG promoter – Rox-STOP-Rox. TITL, TIGRE – Insulators – TRE promoter – LoxP-STOP-LoxP. TIT, TIGRE – Insulators – TRE promoter. EmGFP, Emerald Green Fluorescent Protein. FnGF, FRT – nls-mNeonGreen – FRT. hrGFP, humanized Renilla Green Fluorescent Protein. nT, nls-tdTomato. Syp, Synaptophysin. tdT, tdTomato.

(B) When crossed to the pan-cortical Emx1-IRES-Cre, Ai31 and Ai34 profusely label synaptic terminals by Syp-EmGFP and Syp-tdT, respectively. Native fluorescence was imaged by confocal microcopy in cortex (CTX) and thalamus (TH).

(C) When crossed to Emx1-IRES-Cre, Ai40, Ai80 and Ai86 display pan-cortical native fluorescence for ArchT, CatCh and ArcLight, respectively.

(D) When crossed to the glutamatergic Slc17a7-IRES2-Cre, nls-tdTomato from Ai75 labels extremely brightly all cortical glutamatergic nuclei at age P28. However, by P56 nls-tdTomato expression decreases or appears absent in selected cell populations, and continues to decrease in more cells with time. Similar observations have been made when Ai75 was crossed to other Cre lines. The cause of this phenomenon is unknown. Thus we recommend only short-term usage of the Cre-dependent nuclear labeling by Ai75.

(E) Ai110 was designed as a dual Cre/Flp-dependent reporter to express nls-mNeonGreen (nls-mNG) in cells where only Cre is present, and express nls-tdTomato (nls-tdT) in cells where both Cre and Flp are present. However, there is substantial leaky expression of nls-tdT in the absence of Flp, as seen in Rorb-IRES2-Cre;Ai110 native fluorescence images. The cause of this phenomenon is unknown. On the other hand, the Cre-dependent nls-mNG expression works as expected, as seen in both Rorb-IRES2-Cre;Ai110 and Slc32a1-IRES-Cre;Pvalb-T2A-FlpO;Ai110 native fluorescence images for predominantly layer 4 labeling (Rorb) and pan-GABAergic neuronal labeling (Slc32a1), respectively. The nls-tdT portion can still be useful, as the presence of Flp can turn nls-tdT expression fully on, and this full expression level is clearly distinguishable from the leaky expression (see *Pvalb*-specific nls-tdT labeling in Slc32a1-IRES-Cre;Pvalb-T2A-FlpO;Ai110 in the rightmost panel).

(F) The knock-in Chrm2-tdT fusion protein provides native fluorescence for anatomical boundaries for certain cortical areas such as barrel cortex (SSp-bfd) and primary visual cortex (VISp), visible *in vivo*.

(G) RNA *in situ* hybridization (ISH) with tdT probe shows the cortical layer 4 specificity in a Rorb-T2A-tTA2;Ai63 mouse, in which Ai63 is a tTA-dependent reporter (derived from the Cre/tTA dependent TIGRE1.0 reporter Ai62) expressing tdT from the TRE-tight promoter.

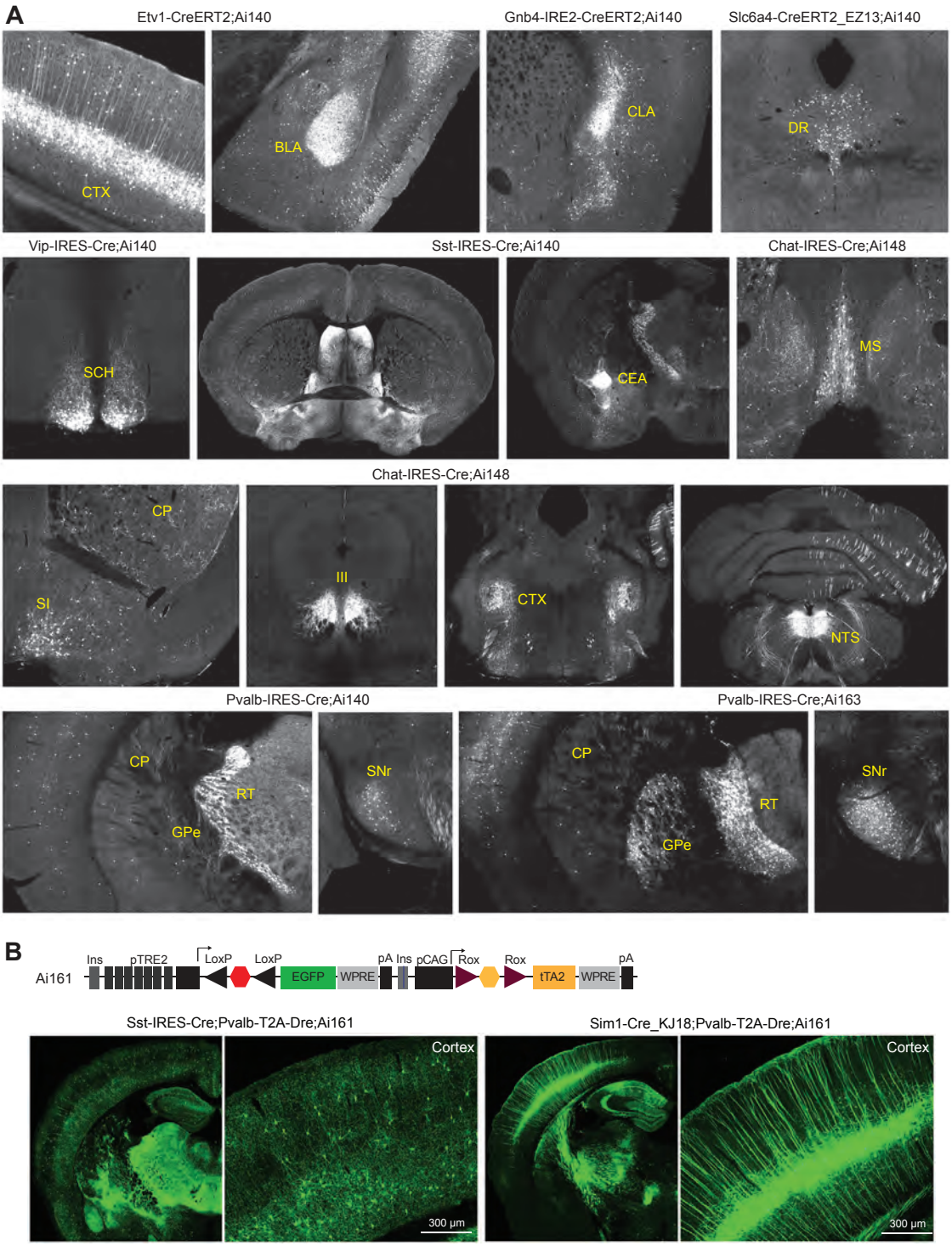

Figure S2. TIGRE2.0 Reporter Lines Exhibit High-Level Transgene Expression across a Wide Range of Cortical and Subcortical Regions When Crossed to a Diverse Set of Cre Driver Lines, Related to Figures 3 and 4

(A) EGFP (in Ai140), GCaMP6f (in Ai148) and GCaMP6s (in Ai163) native fluorescence in various Cre x reporter crosses was imaged by the TissueCyte serial two-photon tomography (STPT) system. Note that more cells are labeled in Pvalb-IRES-Cre;Ai163 than in Pvalb-IRES-Cre;Ai140. BLA, basolateral amygdalar nucleus. CEA, central amygdalar nucleus. CLA, claustrum. CP, caudoputamen. CTX, cortex. DR, dorsal nucleus raphe. GPe, globus pallidus, external segment. III, oculomotor nucleus. MS, medial septal nucleus. NTS, nucleus of the solitary tract. RT, reticular nucleus of the thalamus. SCH, suprachiasmatic nucleus. SI, substantia innominata. SNr, substantia nigra, reticular part. In general, we also noted the presence of Cre-independent, low-level GFP fluorescence which was

(legend continued on next page)

most pronounced in hippocampal excitatory neurons, likely due to the leaky expression from the TRE2 promoter (data not shown), but this should have minimal effect to most applications of these new tools.

(B) We generated a Cre and Dre-dependent GFP-expressing intersectional TIGRE2.0 reporter line: Ai161(TIT2L-GFP-ICR-tTA2) ('R' stands for RoxStop2Rox), in which tTA2 is under Dre control. This line expresses GFP in a Cre- and Dre-dependent manner. Shown here is high-level expression of GFP (imaged by the TissueCyte system) in different neuronal populations defined by two intersectional crosses. In Sst-IRES-Cre;Pvalb-T2A-Dre;Ai161 mice, GFP labels *Sst*+/*Pvalb*+ interneurons, whereas in Sim1-Cre_KJ18;Pvalb-T2A-Dre;Ai161 mice, GFP labels *Pvalb*+ subcortical-projecting layer 5 excitatory neurons. In addition, due to the low-level promiscuous recombination activity of Cre on the Rox sites, in various Cre x Ai161 double transgenic mice, GFP reporter was detected in a small number of cells. This promiscuous recombination occurred more frequently in subcortical areas (data not shown).

Additional notes regarding other attempts to co-express tTA and reporter gene in the TIGRE locus prior to the development of TIGRE2.0 strategy. We first tried two approaches to co-express tTA and a GFP reporter gene, both under Cre control, via a 2A sequence or a bidirectional Bi-Tet promoter, with the hope that upon Cre-mediated recombination, a background level of tTA expression from the TRE or Bi-Tet promoter would initiate a self-amplifying cascade of expression of both tTA and the reporter gene. However, upon Cre transfection of targeted ES clones, we observed no GFP expression (data not shown). Since the TRE promoter we had used was the TRE-Tight version, we then replaced it with the original, 'leakier' tetO promoter (TRE2). In targeted ES clones for both 2A and Bi-Tet versions, we did observe GFP positive cells upon Cre transfection, however, the proportion of green cells was low (data not shown). We went ahead and generated a mouse line from the TRE2-LSL-GFP-2A-tTA2 clone (named Ai109). However, upon crossing Ai109 to 3 Cre lines, Pvalb-IRES-Cre, Nr5a1-Cre and Sst-IRES-Cre, we observed very few GFP-expressing cells in some but not all regions where Cre recombination would normally occur (data not shown). Thus we did not pursue this approach further.

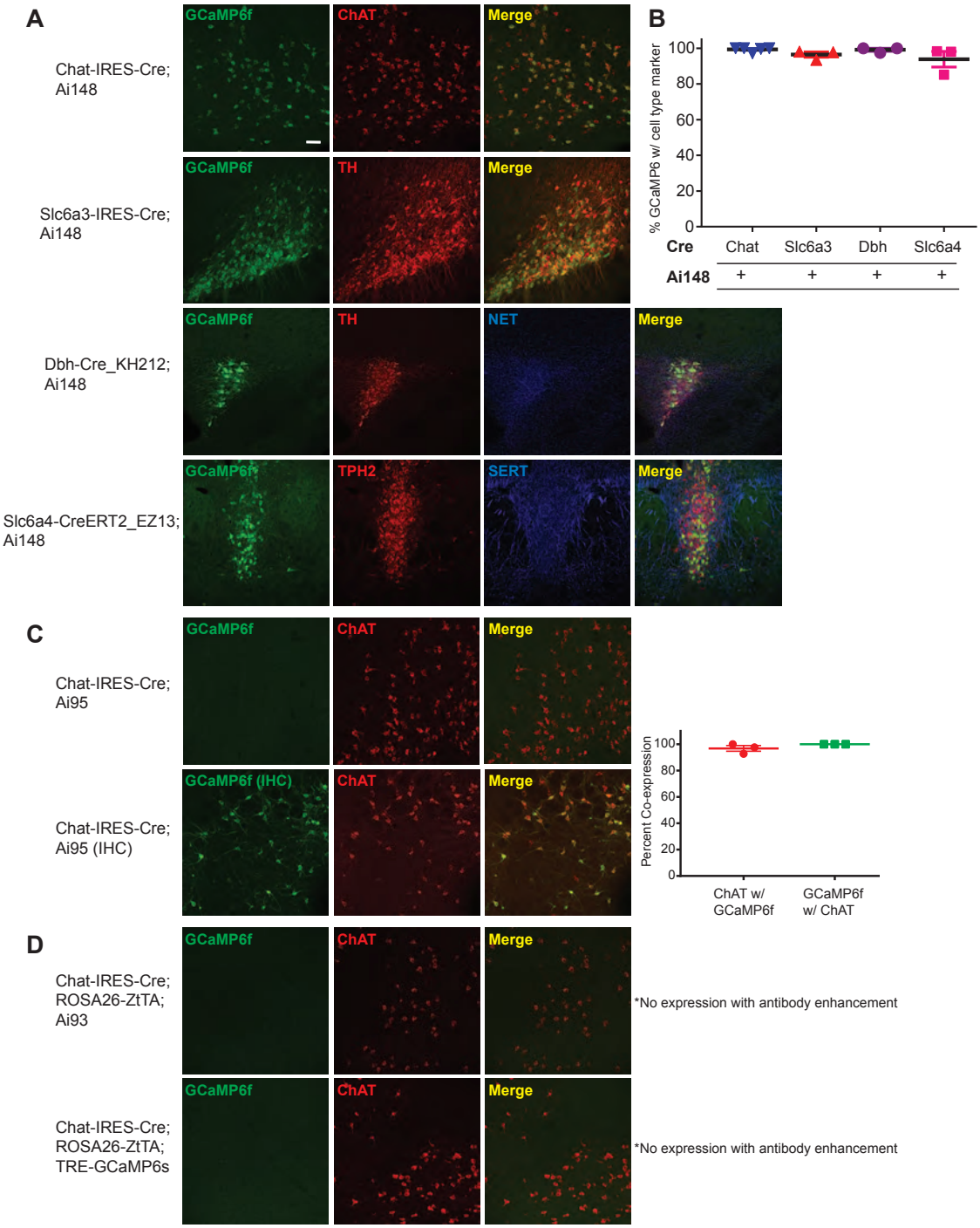

Figure S3. TIGRE2.0-Based Reporter Line Drives Superior Expression of GCaMP6f in Neuromodulatory Cell Types with High Specificity, Related to Figure 3

(A) Representative confocal images show that Ai148 drives specific expression in a variety of neuromodulatory cell types as indicated by co-expression of GCaMP6f with the neuromodulatory cell-type specific markers. The Ai148 reporter line specifically labels cholinergic, choline acetyltransferase (ChAT)-positive neurons in Chat-IRES-Cre cross; dopaminergic, tyrosine hydroxylase (TH)-positive neurons in Slc6a3-IRES-Cre; noradrenergic, TH- and norepinephrine transporter (NET)-positive neurons in Dβh-Cre_KH212; and serotonergic, tryptophan hydroxylase 2 (TPH2)- and serotonin transporter (SERT)-positive neurons in Slc6a4-CreERT2_EZ13. Slc6a4-CreERT2_EZ13;Ai148 mice received 1-day tamoxifen induction after P20 and survived for at least 2 weeks before perfusion. Scale bar: 50 μm.

(B) The TIGRE2.0 reporter line Ai148 labels a subset of cells within each neuromodulatory cell type when crossed with cell-type specific Cre-line (Figures 3H and 3I), and does so with high specify as indicated by co-expression of GCaMP6f with each cell-type specific marker.

(legend continued on next page)

(C) Representative confocal images show that the Rosa26-based Cre reporter line Ai95 expresses GCaMP6f in cholinergic neurons when crossed to Chat-IRES-Cre mice, however, native GCaMP6f fluorescence in fixed sections is undetectable compared to TIGRE2.0 lines (compare panels A and C). In antibody-enhanced sections (IHC), Ai95-driven GCaMP6f expression is specific and widespread among cholinergic neurons as indicated by co-expression of GCaMP6f with choline acetyltransferase (ChAT)-positive neurons. Data are presented as mean ± S.E.M; n = 3 mice.

(D) No GCaMP6f expression is observed in cholinergic neurons from crosses of Chat-IRES-Cre;Rosa26-ZtTA mice with either the TIGRE1.0 line, Ai93 or a different TRE-GCaMP6s reporter (Wekselblatt et al., 2016); n = 2-3 mice per genotype. * No expression can be detected even with immunofluorescence enhancement.

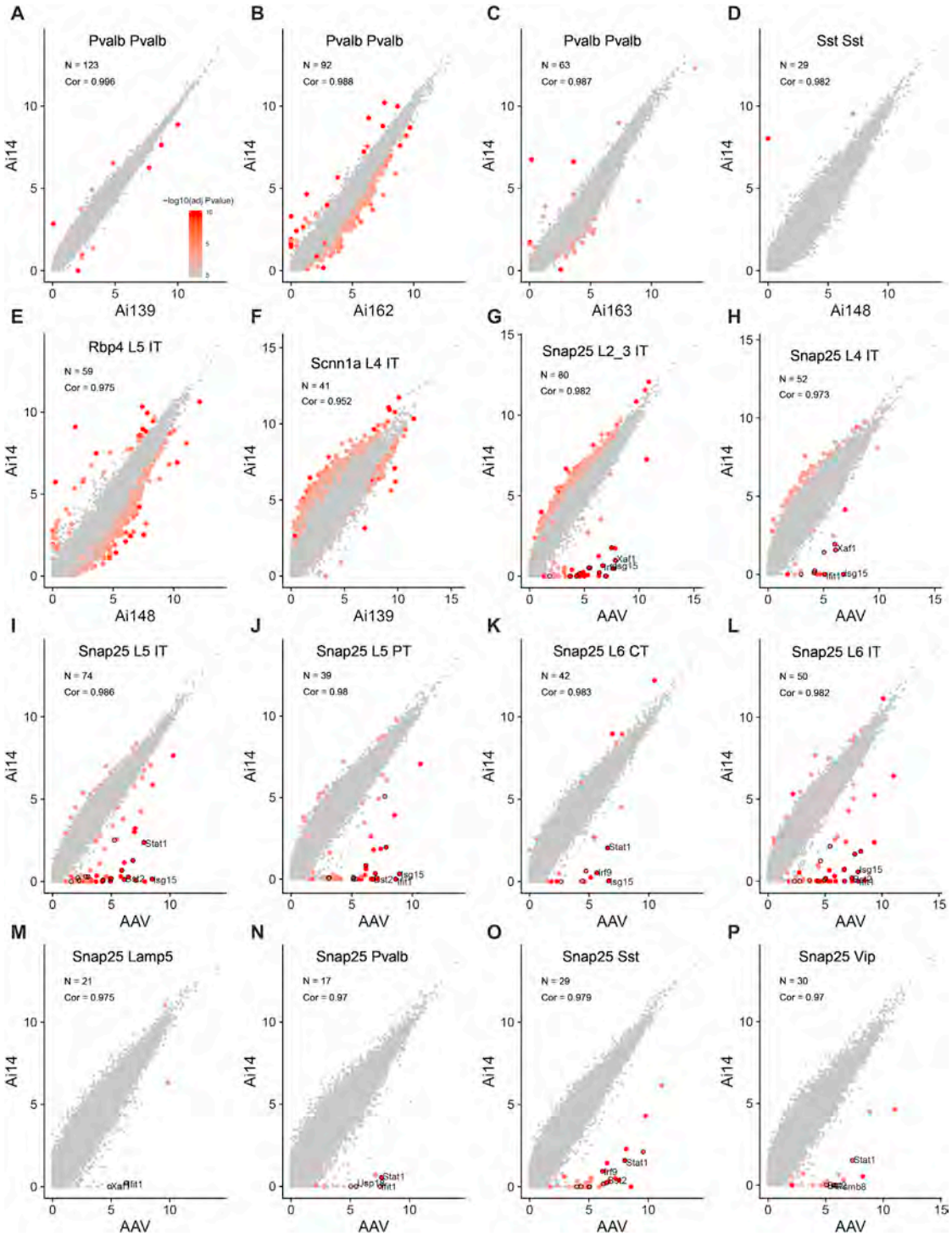

Figure S4. Global Gene Expression Comparison between TIGRE2.0-Labeled or AAV-Infected Neurons and Ai14-Labeled Neurons by scRNA-Seq, Related to Figure 4

(A–F) SMART-Seq v4 datasets from GFP+ (except as noted) cells isolated from Cre x TIGRE2.0 mice were mapped to reference transcriptomic cell types using nearest centroid classifiers. The same number of cells from Cre x Ai14 crosses with matching cell types and genders were chosen as control. Cells with similar cell types were then grouped into cell classes. We tried to detect differentially expressed genes between TIGRE2.0 cells and corresponding Ai14 cells within the same cell class using limma voom mode. X and Y axes correspond to the average counts per million values in log scale, $\log_2$(cpm+1), for cells from Cre x TIGRE2.0 mice and Cre x Ai14 mice, respectively. Genes were colored based on -$\log_{10}$(adjusted P value) to indicate significant changes in expression levels. Mouse lines and cell classes examined are: (A) Pvalb-T2A-CreERT2;Ai139 mouse, *Pvalb*+ cell class, (B) Pvalb-IRES-Cre;Ai162 mouse, *Pvalb*+ cell class, (C) Pvalb-IRES-Cre;Ai163

(legend continued on next page)

mouse, *Pvalb*+ cell class, (D) Sst-IRES-Cre;Ai14;Ai148 mouse, *Sst*+ cell class, (E) Rbp4-Cre_KL100;Ai14;Ai148 mouse, L5 IT cell class (RFP+ cells isolated), and (F) Scnn1a-Tg3-Cre;Ai139 mouse, L4 cell class.

(G–P) SMART-Seq v4 datasets from GFP+ cells isolated from AAV-pCAG-FLEX-GFP-WPRE-pA virus injected Snap25-IRES2-Cre mice were mapped to reference transcriptomic cell types using nearest centroid classifiers. Cells were isolated 3-5 weeks after the AAV injection. The same number of non-AAV infected cells from Cre x Ai14 crosses with matching cell types and genders were chosen as control. Cells belonging to related types were grouped into cell classes. We tried to detect differentially expressed genes between AAV-infected cells and control cells within the same cell class using limma voom mode. X and Y axes correspond to the average counts per million values in log scale, $\log_2$(cpm+1), for AAV-infected cells and corresponding uninfected cells, respectively. Genes are colored based on -$\log_{10}$(adjusted P value) to indicate significant changes in expression levels. A number of genes upregulated in AAV-infected cells belong to a Type I interferon responsive group (GO: 0034340), and they are highlighted by black circles. The top 3 differentially expressed genes from this group are labeled by their names. Cell classes examined are shown on the label for each panel (to the right of Snap25).

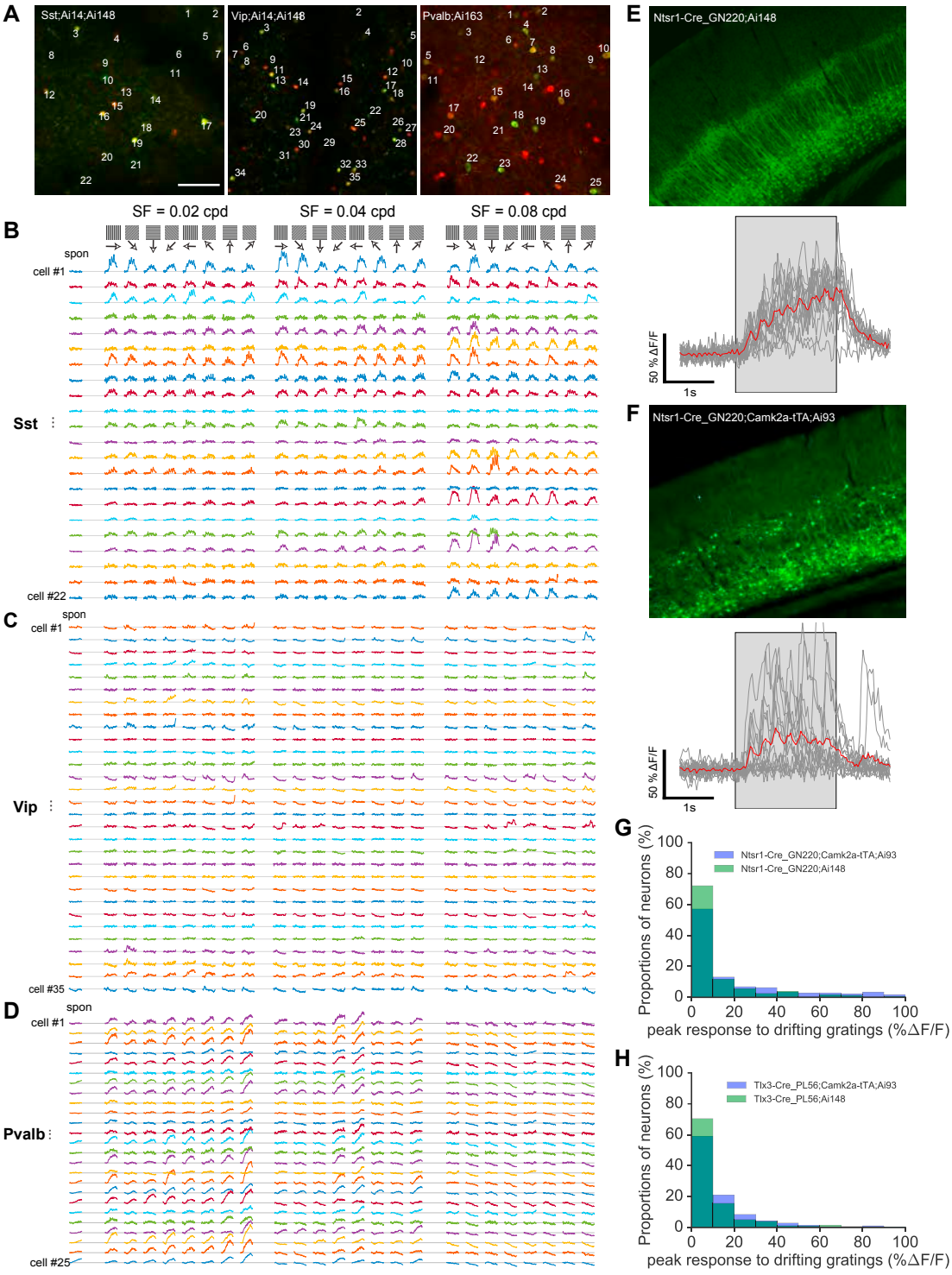

Figure S5. Strong Visually Evoked Calcium Responses in Cortical Inhibitory and Excitatory Neurons Reported by TIGRE2.0 Mice, Related to Figure 5

(A) Two-photon calcium imaging Z-projection images (from time series) showing red fluorescence (tdT) and green fluorescence (GCaMP6) in Sst-IRES-Cre;Ai14;Ai148, Vip-IRES-Cre;Ai14;Ai148 and Pvalb-IRES-Cre;Ai163 mice.

(B–D) Orientation tuning properties derived from the ΔF/F responses of 22 individual *Sst*+ cells from the Sst-IRES-Cre;Ai14;Ai148 mouse (B), 35 *Vip*+ cells from Vip-IRES-Cre;Ai14;Ai148 (C) and 25 *Pvalb*+ cells from Pvalb-IRES-Cre;Ai163 (D). The visual response mapping was performed with whole-screen sinusoidal

(legend continued on next page)

drifting gratings showing 8 orientations (0° to 315° in 45° increments), 5 spatial frequencies (0.01, 0.02, 0.04, 0.08 and 0.16 cycle per degree) and 1 temporal frequency (2 Hz), presented at 80% contrast in a random sequence for 8 repetitions (STAR Methods).

(E–H) Comparison of visually evoked calcium responses in excitatory neurons of deep cortical layers in Ai148 and Ai93 mice. (E) A representative coronal section in VISp of an Ntsr1-Cre_GN220;Ai148 mouse showing GCaMP6f expression in layer 6 neurons specifically, and example neuronal responses to drifting gratings for a cell recorded in this mouse. The red trace represents the average response. (F) A representative coronal section in VISp of an Ntsr1-Cre_GN220;Camk2a-tTA;Ai93 mouse showing GCaMP6f expression in layer 6 neurons as well as some upper layer neurons, and example neuronal responses to drifting gratings for a cell recorded in this mouse. The red trace represents the average response. (G) Distribution of peak amplitudes of visually evoked responses to drifting gratings for all cells recorded in Ntsr1-Cre_GN220 mice (total of 183 cells in Ntsr1-Cre_GN220;Camk2a-tTA;Ai93, and 310 cells in Ntsr1-Cre_GN220;Ai148 mice). (H) Distribution of peak amplitudes of visually evoked responses to drifting gratings for all cells recorded in another Cre line, Tlx3-Cre_PL56, which drives GCaMP6f expression in cortical layer 5 neurons (total of 281 cells in Tlx3-Cre_PL56;Camk2a-tTA;Ai93, and 349 cells in Tlx3-Cre_PL56;Ai148 mice).

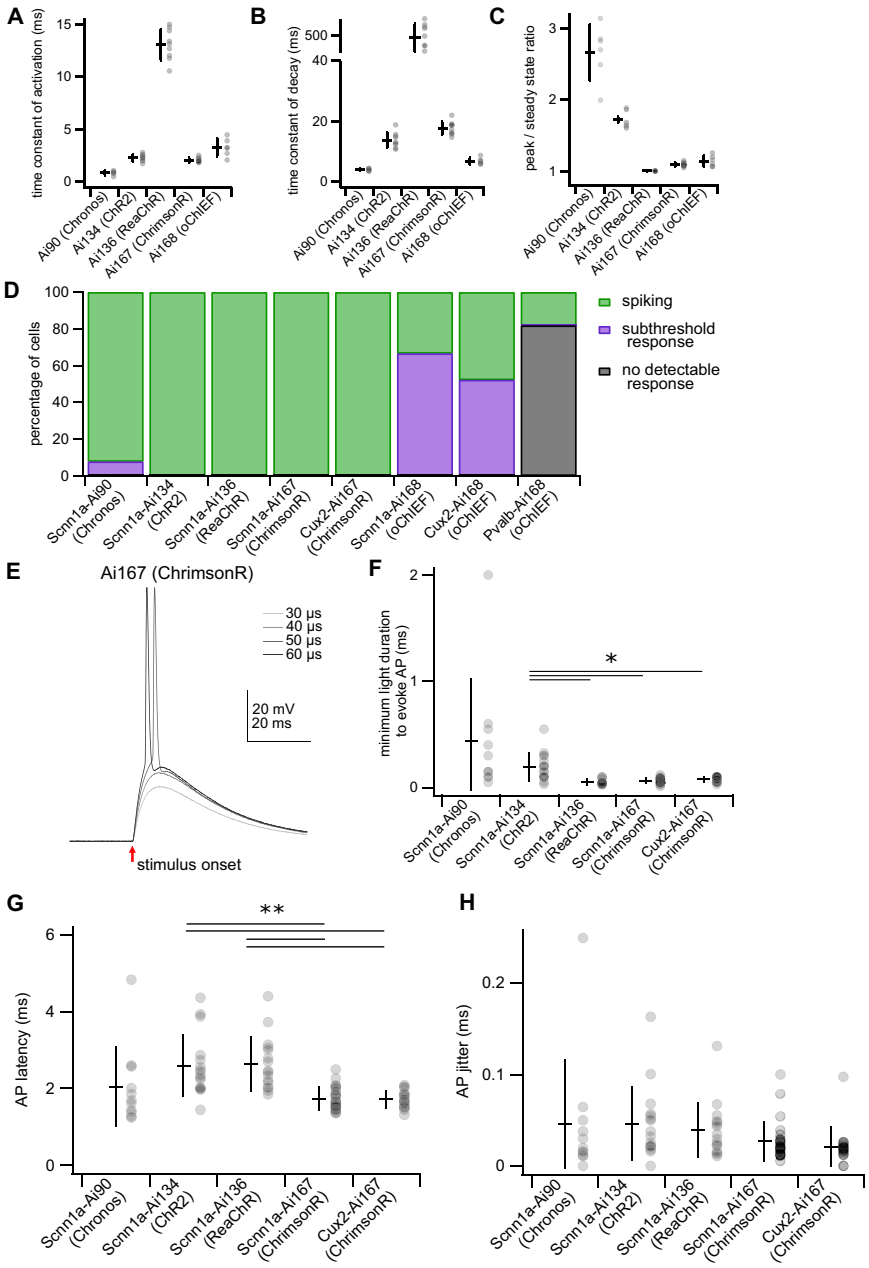

Figure S6. Characterization of Light-Evoked Responses for Ai90, Ai134, Ai136, Ai167, and Ai168 Transgenic Lines, Related to Figure 6

In addition to mouse strains described in Figure 6, also examined are Cux2-CreERT2;Ai167 and Cux2-CreERT;Ai168 expressing ChrimsonR and oChIEF, respectively, in cortical layer 2/3 excitatory neurons. We also examined Pvalb-IRES-Cre;Ai168 mice expressing oChIEF in Pvalb+ interneurons. For all data presented here, neurons recorded from Ai90, Ai134 and Ai168 animals were stimulated with 470 nm light, whereas experiments characterizing Ai136 and Ai167 mice used 590 nm light.

(A) Time constants of activation measured by a mono-exponential fit from the onset of the light pulse to the peak of the photocurrent (see Figure 6A). Ai90: 0.81 ± 0.21 ms; Ai134: 2.3 ± 0.3 ms; Ai136: 13.1 ± 1.5 ms; Ai167: 2.0 ± 0.2 ms; Ai168 3.3 ± 0.8 ms. $p < 0.001$ for all comparisons except: Ai134 versus Ai167; Ai134 versus Ai168 and Ai167 versus Ai168.

(B) Time constants of de-activation measured by a mono-exponential fit from the termination of the light pulse to the return of the current to baseline (see Figure 6A). Ai90: 3.8 ± 0.4 ms; Ai134: 13.7 ± 2.5 ms; Ai136: 478 ± 166 ms; Ai167: 17.6 ± 2.2 ms; Ai168: 6.6 ± 1.1 ms. $p < 0.0005$ for all comparisons.

(C) Peak/steady-state ratio. Steady-state was measured as the average current amplitude during the final 5 ms of the 100 ms light exposure (see Figure 6A). Ai90: 2.66 ± 0.39; Ai134: 1.72 ± 0.04; Ai136: 1.01 ± 0.003; Ai167: 1.10 ± 0.03; Ai168 1.14 ± 0.08 (n = 6-10 cells for each group in panels A-C). $p < 0.005$ for all comparisons except: Ai136 versus Ai168 and Ai167 versus Ai168.

(D) Percentage of cells in each transgenic line displaying action potential (AP) firing, subthreshold response or no response to optical stimulation. We first tested the ability of each neuron to generate light-evoked APs with 1 ms light pulses. If AP firing was not observed, light exposure was prolonged (up to 50 ms) to further

(legend continued on next page)

test the sensitivity of the cell to optical stimulation. Except for the Ai168 lines, nearly all cells fired in response to a 1 ms light pulse (see panel F).
(E) Representative responses of a Scnn1a-Cre;Ai167 cell to saturating light pulses of increasing duration.
(F) Minimum light durations required to evoke an AP for each transgenic line. Minimum duration in Ai90: 0.44 ± 0.58 ms; Ai134: 0.19 ± 0.13 ms; Ai136: 0.052 ± 0.027 ms; Scnn1a-Ai167: 0.065 ± 0.026 ms; Cux2-Ai167: 0.078 ± 0.025 ms.
(G) Latency of spiking in response to a 1 ms saturating light pulse. Ai90: 2.0 ± 1.0 ms; Ai134: 2.6 ± 0.8 ms; Ai136: 2.6 ± 0.7 ms; Scnn1a-Ai167: 1.7 ± 0.3 ms; Cux2-Ai167: 1.7 ± 0.2 ms.
(H) Jitter of spiking in response to a 1 ms saturating light pulse. Ai90: 46 ± 70 μs; Ai134: 46 ± 40 μs; Ai136: 39 ± 30 μs; Scnn1a-Ai167: 27 ± 22 μs; Cux2-Ai167: 21 ± 21 μs. All data within this figure are plotted as the mean ± standard deviation. *$p < 0.001$; **$p < 0.0001$. n = 10-16 cells per transgenic line.

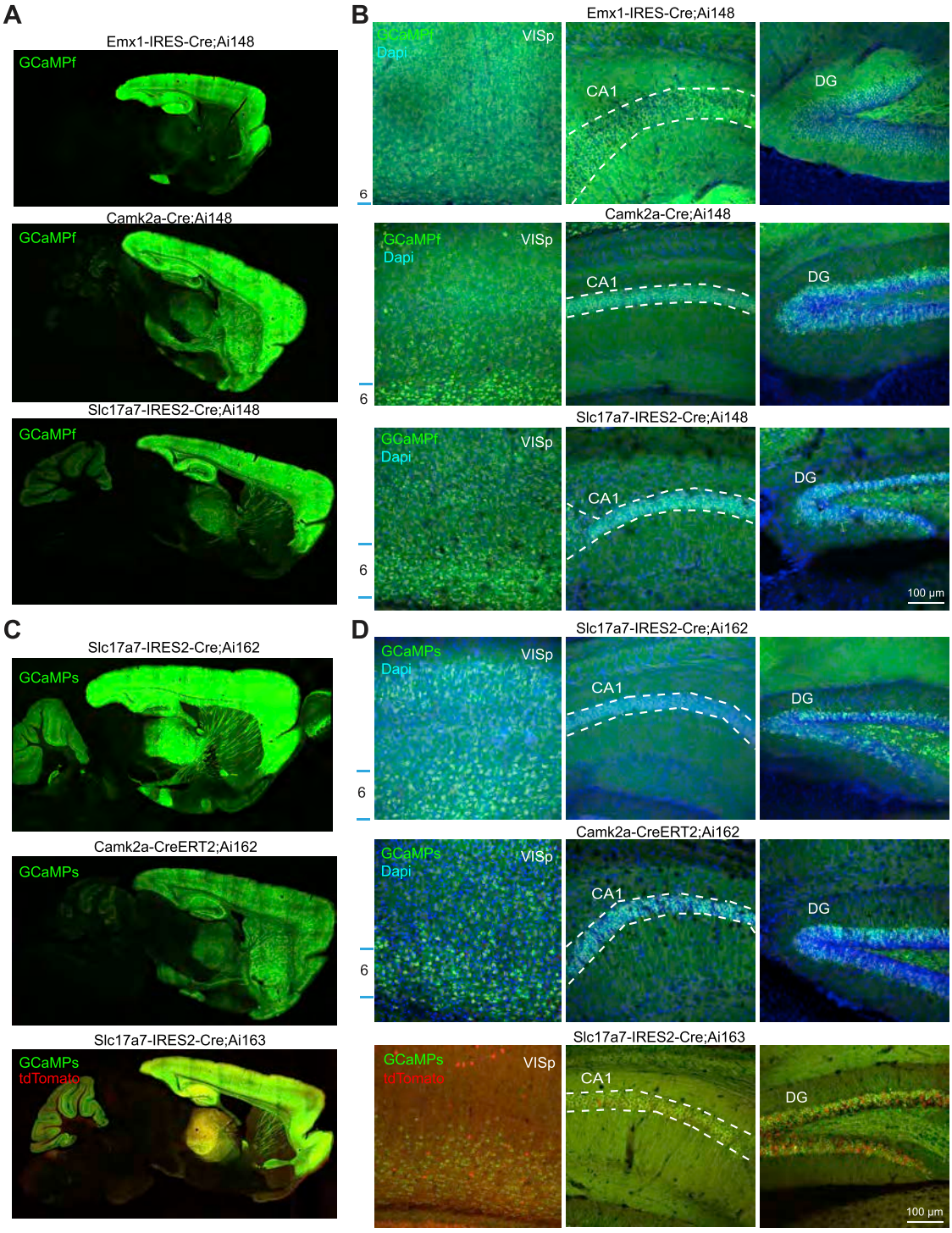

Figure S7. Adverse Effects Associated with Strong and Broad Transgene Expression, Related to Figure 7

(A–D) Representative confocal images of native GCaMP6f, GCaMP6s, or tdTomato fluorescence from Ai148 (A-B), Ai162 and Ai163 (C-D) mice crossed to various cortical pan-excitatory Cre lines. Expression throughout the brain, in the primary visual cortex (VISp) and within hippocampal subfields (CA1 and dentate gyrus) is shown. The approximate location of layer 6 within the cortex and the pyramidal layer of CA1 (between dashed lines) are annotated in the 20X images. All montage and 20X images were acquired using the same instrument settings.

In double transgenic animals containing Ai148 and Emx1-IRES-Cre (which mediates pan-cortical and pan-hippocampal expression potentially starting as early as embryonic day E9), GCaMP6f fluorescence was extremely bright, the cortex appeared thinner and the hippocampus was smaller. The mice also had reduced body weight and died prematurely (typically around 1-3 months of age). To investigate if these phenotypes were due to the widespread and developmental

(legend continued on next page)

expression of GCaMP6f or tTA2, we fed the mice doxycycline-containing chow throughout the pregnancy and animal's lifetime. This treatment did not ameliorate the adverse phenotypes (data not shown), suggesting that the observed effects were likely due to the widespread developmental expression of tTA2, a potent transcriptional activator. Furthermore, we observed the same phenotypes when Ai140 was crossed with Emx1-IRES-Cre, which expresses a more innocuous molecule (GFP) rather than a calcium buffer (GCaMP6f).

To determine if tTA2 would be better tolerated if expressed later in development, we generated double-transgenic mice containing Ai148, Ai162 or Ai163 and one of pan-cortical Cre lines with later developmental onset, such as Slc17a7-IRES2-Cre, Camk2a-Cre and Camk2a-CreERT2. Encouragingly, double-transgenic animals from the majority of these crosses had no gross behavioral phenotype and the brains appeared largely normal, with the exception of Camk2a-Cre;Ai148 and Slc17a7-IRES2-Cre;Ai148 animals. The cortex from these animals appeared thinner and the dentate gyrus of the latter had notable disorganization.

To obtain pan-GABAergic expression, we crossed Ai139, Ai140, and Ai148 reporters with Gad2-IRES-Cre, but never obtained any double positive transgenic mice after genotyping dozens of pups, suggesting embryonic lethality (Table S5). It is unclear how Gad2-IRES-Cre expression led to lethality, given that double transgenic mice for other interneuron Cre lines (i.e., Pvalb, Sst and Vip) all appeared normal. We also extremely rarely obtained double transgenic mice for Ai140 and Sim1-Cre_KJ18, suggesting perinatal lethality; the few double transgenic mice that survived had forelimb atrophy (Table S5). Sim1-Cre_KJ18 is a BAC transgenic Cre line that, when crossed to Ai14, gives rise to a specific recombination pattern in the adult brain (which is a cumulative representation of all recombination events in the animal's life) that is restricted to only a few places – cortical layer 5b, pontine gray, nucleus of the lateral olfactory tract, and parts of hypothalamus and medial amygdala. We suspect that the lethality might be due to expression of tTA2 in other, so far unknown body regions. Collectively, these data and our results with the pan-excitatory crosses, suggest that extremely high tTA2 levels are not well tolerated when broadly expressed in CNS, early in development and/or potentially outside of the CNS. We caution users against using Cre lines with widespread and early developmental expression and suggest using the more specific Cre lines in which we have not observed any adverse phenotypes.

Cell, Volume *174*

Supplemental Information

A Suite of Transgenic Driver and Reporter Mouse Lines with Enhanced Brain-Cell-Type Targeting and Functionality

Tanya L. Daigle, Linda Madisen, Travis A. Hage, Matthew T. Valley, Ulf Knoblich, Rylan S. Larsen, Marc M. Takeno, Lawrence Huang, Hong Gu, Rachael Larsen, Maya Mills, Alice Bosma-Moody, La' Akea Siverts, Miranda Walker, Lucas T. Graybuck, Zizhen Yao, Olivia Fong, Thuc Nghi Nguyen, Emma Garren, Garreck H. Lenz, Mariya Chavarha, Julie Pendergraft, James Harrington, Karla E. Hirokawa, Julie A. Harris, Philip R. Nicovich, Medea J. McGraw, Douglas R. Ollerenshaw, Kimberly A. Smith, Christopher A. Baker, Jonathan T. Ting, Susan M. Sunkin, Jérôme Lecoq, Michael Z. Lin, Edward S. Boyden, Gabe J. Murphy, Nuno M. da Costa, Jack Waters, Lu Li, Bosiljka Tasic, and Hongkui Zeng

Table S1. Driver lines generated by the Allen Institute for Brain Science. Related to **Figure 1**.

Line	JAX stock #	Transgenic type	Reference
A930038C07Rik-Tg1-Cre	017346	BAC random insertion	Harris et al., 2014
Adcyap1-F2A-Cre	030155	Knock-in at Stop codon	Harris et al., 2014
Avp-IRES2-Cre	023530	Knock-in at Stop codon	Harris et al., 2014
Camk2a-CreERT2	012362	Random insertion	Madisen et al., 2010
Cart-Tg1-Cre	009615	BAC random insertion	Harris et al., 2014
Ctgf-T2A-dgCre	028535	Knock-in at Stop codon	Tasic et al., 2016
Erbb4-F2A-CreERT2	012360	Knock-in at Stop codon	Madisen et al., 2010
Gnb4-IRES2-Cre	029587	Knock-in at Stop codon	Wang et al., 2017
Ndnf-IRES2-dgCre	028536	Knock-in at Stop codon	Tasic et al., 2016
Nr4a2-SA-IRES-Dre		Knock-in at 2nd intron?	Madisen et al., 2015
Ntng2-IRES2-Cre	029588	Knock-in at Stop codon	Wang et al., 2017
Nxph4-T2A-CreERT2	022861	Knock-in at Stop codon	Harris et al., 2014
Penk-F2A-CreERT2	022862	Knock-in at Stop codon	Harris et al., 2014
Pvalb-T2A-Cre	012358	Knock-in at Stop codon	Madisen et al., 2010
Pvalb-T2A-CreERT2	021189	Knock-in at Stop codon	Harris et al., 2014
Pvalb-T2A-dCre	022863	Knock-in at Stop codon	Harris et al., 2014
Pvalb-T2A-Dre	021190	Knock-in at Stop codon	Madisen et al., 2015
Pvalb-T2A-FlpE	021191	Knock-in at Stop codon	Madisen et al., 2015
Pvalb-T2A-FlpO	022730	Knock-in at Stop codon	Madisen et al., 2015
Rasgrf2-T2A-dCre	022864	Knock-in at Stop codon	Harris et al., 2014
Rorb-IRES2-Cre	023526	Knock-in at Stop codon	Harris et al., 2014
Rorb-T2A-tTA2	028537	Knock-in at Stop codon	Madisen et al., 2015
Scnn1a-Tg1-Cre	009111	BAC random insertion	Madisen et al., 2010
Scnn1a-Tg2-Cre	009112	BAC random insertion	Madisen et al., 2010
Scnn1a-Tg3-Cre	009613	BAC random insertion	Madisen et al., 2010
Slc17a7-IRES2-Cre	023527	Knock-in at Stop codon	Harris et al., 2014
Snap25-IRES2-Cre	023525	Knock-in at Stop codon	Harris et al., 2014
Sst-Cre		Knock-in at Start codon	Harris et al., 2014
Tac1-IRES2-Cre	021877	Knock-in at Stop codon	Harris et al., 2014
Tac2-IRES2-Cre	021878	Knock-in at Stop codon	Harris et al., 2014
Trib2-F2A-CreERT2	022865	Knock-in at Stop codon	Harris et al., 2014
Wfs1-Tg2-CreERT2	009614	BAC random insertion	Madisen et al., 2010
Wfs1-Tg3-CreERT2	009103	BAC random insertion	Madisen et al., 2010
Calb1-IRES2-Cre	028532	Knock-in at Stop codon	This paper
Calb1-T2A-dgCre	023531	Knock-in at Stop codon	This paper
Cart-IRES2-Cre	028533	Knock-in at Stop codon	This paper
Esr2-IRES2-Cre	030158	Knock-in at Stop codon	This paper
Fezf1-T2A-dCre	025110	Knock-in at Stop codon	This paper
Gnb4-IRES2-CreERT2	030159	Knock-in at Stop codon	This paper
Htr1a-IRES2-Cre	030160	Knock-in at Stop codon	This paper
Npr3-IRES2-Cre	031333	Knock-in at Stop codon	This paper
Npy-IRES2-FlpO	030211	Knock-in at Stop codon	This paper
Oxtr-T2A-Cre	031303	Knock-in at Stop codon	This paper
Pdyn-T2A-CreERT2	030197	Knock-in at Stop codon	This paper
Penk-IRES2-Cre-neo	025112	Knock-in at Stop codon	This paper
Plxnd1-IRES2-dgFlpO		Knock-in at Stop codon	This paper
Rasgrf2-T2A-dgFlpO	029589	Knock-in at Stop codon	This paper
Rorb-IRES2-FlpO	029590	Knock-in at Stop codon	This paper
Rorb-P2A-FlpO		Knock-in at Stop codon	This paper
Slc17a6-IRES2-FlpO	030212	Knock-in at Stop codon	This paper
Slc17a8-IRES2-Cre	028534	Knock-in at Stop codon	This paper
Slc32a1-IRES2-FlpO	031331	Knock-in at Stop codon	This paper
Slc32a1-T2A-FlpO	029591	Knock-in at Stop codon	This paper
Tacr1-T2A-Cre		Knock-in at Stop codon	This paper
Tnnt1-IRES2-CreERT2		Knock-in at Stop codon	This paper
Vipr2-IRES2-Cre	031332	Knock-in at Stop codon	This paper

Table S2. Reporter lines generated by the Allen Institute for Brain Science. Related to **Figures 2** and **3**.

Line	JAX stock #	Knock-in locus	Reference
Ai2(RCL-EYFP)	007920	ROSA26	Madisen et al., 2010
Ai3(RCL-EYFP)	007903	ROSA26	Madisen et al., 2010
Ai6(RCL-ZsGreen)	007906	ROSA26	Madisen et al., 2010
Ai9(RCL-tdT)	007909	ROSA26	Madisen et al., 2010
Ai14(RCL-tdT)	007914	ROSA26	Madisen et al., 2010
Ai27(RCL-ChR2H134R-tdT)	012567	ROSA26	Madisen et al., 2012
Ai32(RCL-ChR2H134R-EYFP)	012569, 024109	ROSA26	Madisen et al., 2012
Ai35(RCL-Arch-EGFP-ER2)	012735	ROSA26	Madisen et al., 2012
Ai38(RCL-GCaMP3)	014538	ROSA26	Zariwala et al., 2012
Ai39(RCL-eNpHR3.0-EYFP)	014539	ROSA26	Madisen et al., 2012
Ai57(RCFL-Jaws)		ROSA26	Madisen et al., 2015
Ai62(TITL-tdT)	022731	TIGRE	Madisen et al., 2015
Ai65(RCFL-tdT)	021875	ROSA26	Madisen et al., 2015
Ai66(RCRL-tdT)	021876	ROSA26	Madisen et al., 2015
Ai72(RCL-VSFPB)		ROSA26	Madisen et al., 2015
Ai78(TITL-VSFPB)	023528	TIGRE	Madisen et al., 2015
Ai79(TITL-Jaws)	023529	TIGRE	Madisen et al., 2015
Ai82(TITL-GFP)	023532	TIGRE	Madisen et al., 2015
Ai85(TITL-iGluSnFr)	026260	TIGRE	Madisen et al., 2015
Ai87(RCL-iGluSnFr)		ROSA26	Madisen et al., 2015
Ai92(TITL-YCX2.60)	026262	TIGRE	Madisen et al., 2015
Ai93(TITL-GCaMP6f)	024103	TIGRE	Madisen et al., 2015
Ai94(TITL-GCaMP6s)	024104	TIGRE	Madisen et al., 2015
Ai95(RCL-GCaMP6f)	024105	ROSA26	Madisen et al., 2015
Ai96(RCL-GCaMP6s)	024106	ROSA26	Madisen et al., 2015
Snap25-LSL-F2A-GFP	021879	Snap25	Madisen et al., 2015
Snap25-T2A-GCaMP6s	025111	Snap25	Madisen et al., 2015
TITL-RCaMP1.07	030217	TIGRE	Bethge et al., 2017
Ai31(RCL-Syp-EmGFP)		ROSA26	This paper
Ai34(RCL-Syp-tdT)	012570	ROSA26	This paper, see also Abraira et al., 2017
Ai40(RCL-ArchT-EGFP)	021188	ROSA26	This paper
Ai47(RCL-triGFP)		ROSA26	This paper, see also Steinecke et al., 2017
Ai63(TIT-tdT)		TIGRE	This paper
Ai65F(RCF-tdT)		ROSA26	This paper
Ai66R(RCR-tdT)		ROSA26	This paper
Ai75(RCL-nT)	025106	ROSA26	This paper
Ai80(RCFL-CatCh)	025109	ROSA26	This paper
Ai86(TITL-ArcLight)		TIGRE	This paper
Ai90(TITL-Chronos)	024100	TIGRE	This paper
Ai110(RCL-FnGF-nT)		ROSA26	This paper
Ai133(TITL-ssAPEX2tm)	030213	TIGRE	This paper
Ai134(TITL-ChR2-YFP)	031334	TIGRE	This paper
Ai136(TITL-ReaChR-YFP)	030216	TIGRE	This paper
Ai139(TIT2L-GFP-ICL-TPT)	030219	TIGRE	This paper
Ai140(TIT2L-GFP-ICL-tTA2)	030220	TIGRE	This paper
Ai148(TIT2L-GC6f-ICL-tTA2)	030328	TIGRE	This paper, see also Hsiang et al., 2017
Ai161(TIT2L-GFP-ICR-tTA2)	031561	TIGRE	This paper
Ai162(TIT2L-GC6s-ICL-tTA2)	031562	TIGRE	This paper
Ai163(TIT2L-GC6s-ICL-TPT)		TIGRE	This paper
Ai167(TIT2L-ChrimsonR-tdT-ICL-tTA2)		TIGRE	This paper
Ai168(TIT2L-oChIEF-P2A-tdT-ICL-tTA2)		TIGRE	This paper
Ai169(TIT2L-ASAP2s-ICL-tTA2)	031569	TIGRE	This paper
Ai170(TIT2L-ASAP2s-Kv-ICL-tTA2)	031570	TIGRE	This paper
Chrm2-tdT	030330	Chrm2	This paper

Acronyms: RCL, Rosa26 – CAG promoter – LoxP-STOP-LoxP. **RCFL**, Rosa26 – CAG promoter – FRT-STOP-FRT – LoxP-STOP-LoxP. **RCRL**, Rosa26 – CAG promoter – Rox-STOP-Rox – LoxP-STOP-LoxP. **RCF**, Rosa26 – CAG promoter – FRT-STOP-FRT. **RCR**, Rosa26 – CAG promoter – Rox-STOP-Rox. **LSL**, LoxP-STOP-LoxP. **TITL**, TIGRE – Insulators – TRE promoter – LoxP-STOP-LoxP. **TIT**, TIGRE – Insulators – TRE promoter. **TIT2L**, TIGRE – Insulators – TRE2 promoter – LoxP-STOP-LoxP. **ICL**, Insulators – CAG promoter – Lox2272-STOP2-Lox2272. **ICR**, Insulators – CAG promoter – Rox-STOP2-Rox. **FnGF**, FRT – nls-mNeonGreen – FRT. **GC6f**, GCaMP6f. **GC6s**, GCaMP6s. **nT**, nls-tdTomato. **Syp**, Synaptophysin. **tdT**, tdTomato. **TPT**, tdTomato-P2A-tTA2.

Table S3. Driver lines expressing trimethoprim (TMP)-inducible Cre or FlpO. Recombination patterns examined in adult mice (P56 or older) with drivers crossed to either a Cre reporter Ai14 or a Flp reporter Ai65F. Related to **Figure 1**.

Driver line	No TMP induction	With TMP induction in adult stage
Calb1-T2A-dgCre	Significant baseline level but not full recombination pattern	Full recombination pattern resembling that of the endogenous gene
Ctgf-T2A-dgCre	Very sparse baseline recombination	Full recombination pattern resembling that of the endogenous gene
Fezf1-T2A-dCre	Full recombination pattern resembling that of the endogenous gene, same as with TMP induction	Full recombination pattern resembling that of the endogenous gene, same as without TMP induction
Ndnf-IRES2-dgCre	Full recombination pattern resembling that of the endogenous gene, same as with TMP induction	Full recombination pattern resembling that of the endogenous gene, same as without TMP induction
Pvalb-T2A-dCre	Significant baseline level but not full recombination pattern	Full recombination pattern resembling that of the endogenous gene
Rasgrf2-T2A-dCre	Sparse baseline recombination	Full recombination pattern resembling that of the endogenous gene
Plxnd1-IRES2-dgFlpO	No recombination	Very sparse recombination pattern as a subset of that of the endogenous gene
Rasgrf2-T2A-dgFlpO	No recombination	Scattered recombination pattern as a subset of that of the endogenous gene

Table S4. Protein sequence of soma-enriched voltage sensor ASAP2s-Kv. Related to **Figure 4**.

The ASAP2s segment is labeled in green, with the circularly permuted GFP sequence underlined. The 65 amino acid segment from the C-terminus of the rat Kv2.1 potassium channel (orange) was fused to the C-terminus of ASAP2s via a flexible linker (blue). Black letters correspond to enzymatic restriction sites. Distinct elements of the protein are color-coded. This segment is sufficient to target a heterologous protein to neuronal soma and proximal dendrites and has been repeatedly used for soma targeting of opsins.

ASAP2s-Kv sequence
METTVRYEQGSELTKTSSSPTADEPTIKIDDGRDEGNEQDSCSNTIRRKISPFVMSFGFRVFGVVLIIVDIIVVIVDLAISEK KRGIREILEGVSLAIALFFLVDVLMRVFVEGFKNYFRSKLNTLDAVIVVGTLLINMTYSFSDLAAFNSHNVYITADKQKNGIK ANFTVRHNVEDGSVQLADHYQQNTPIGDGPVLLPDNHYLSTQTVLSKDPNEKRDHMVLLEFVTAAGITHGMDELYGGTGGSAS QGEELFTGVVPILVELDGDVNGHKFSVRGEGEGDATIGKLTLKFICTTGKLPVPWPTLVTTLTYGVQCFSRYPDHMKRHDFFK SAMPEGYVQERTISFKDDGKYKTRAVVKFEGDTLVNRIELKGTDFKEDGNILGHKLEYNTDQMPQMVTLLRVLRIVILIRIFQ LASQKKQLEVVTLKGSSGSSGSSTRQSQPILNTKEMAPQSKPPEELEMSSMPSPVAPLPARTEGVIDMRSMSSIDSFISCATD FPEATRF

Table S5. Problematic reporter and driver line crosses. Related to **Figure 7**.

Reporter	Driver	Genotype	Phenotype
Ai139	Gad2-IRES-Cre	Ai139/wt; Gad2-IRES-Cre/wt	Embryonic lethal
Ai140	Gad2-IRES-Cre	Ai140/wt; Gad2-IRES-Cre/wt	Embryonic lethal
Ai148	Gad2-IRES-Cre	Ai148/wt; Gad2-IRES-Cre/wt	Embryonic lethal
Ai136	Sim1-Cre_KJ18, ROSA26-ZtTA	Ai139/wt; Sim1-Cre_KJ18/wt; ROSA26-ZtTA/wt	Embryonic lethal
Ai140	Sim1-Cre_KJ18	Ai140/wt; Sim1-Cre_KJ18/wt	Embryonic lethal
Ai140	Emx1-IRES-Cre	Ai140/wt;Emx1-IRES-Cre/wt	Reduced body weight and brain size, thinned cortex, substantial neurodegeneration in hippocampal subfields, and high premature mortality rate; doxycycline treatment (to suppress GFP expression) did not reverse phenotype
Ai148	Emx1-IRES-Cre	Ai148/wt; Emx1-IRES-Cre/wt	Reduced body weight and brain size, thinned cortex, substantial neurodegeneration in hippocampal subfields, and high premature mortality rate; doxycycline treatment (to suppress GCaMP6f expression) did not reverse phenotype
Ai148	Camk2a-Cre	Ai148/wt; Camk2a-Cre/wt	Reduced brain size and some neurodegeneration in hippocampal subfields
Ai148	Slc17a7-IRES2-Cre	Ai148/wt; Slc17a7-IRES2-Cre/wt	Reduced brain size and some neurodegeneration in hippocampal subfields
Ai148	Sst-IRES-Cre	Ai148/wt; Sst-IRES-Cre/wt	Ulcerative dermatitis (most commonly in anogenital region, lower jaw, and sternum), with occasional rectal prolapse and/or seizure, seen in ~30% mice with an average onset at ~P100
Ai168	Pvalb-IRES-Cre	Ai168/wt; Pvalb-IRES-Cre/wt	Reduced body weight, head tilt and atrophy of hind limbs; phenotype can be ameliorated by doxycycline treatment
Ai75	Snap25-IRES2-Cre	Ai75/wt; Snap25-IRES2-Cre/wt	Premature death (around 4 weeks of age)

Table S6. All observations of normal and aberrant cortical activity in cortical pan-excitatory GCaMP6 expressing lines. Related to **Figure 7**.

Animals with aberrant activity are highlighted (gray), observations with aberrant activity are highlighted in red, with the corresponding sex and age of animals at the time of each observation. We found no relationship between these events and the age of the animal.

Genotype	Mouse ID#	Sex	Age at observation (postnatal days)
Slc17a7-IRES2-Cre;Ai162	292915	F	52
Slc17a7-IRES2-Cre;Ai162	292917	F	52
Slc17a7-IRES2-Cre;Ai162	297312	M	110
Slc17a7-IRES2-Cre;Ai162	297310	M	110
Slc17a7-IRES2-Cre;Ai162	304572	F	170
Slc17a7-IRES2-Cre;Ai162	315689	F	120
Slc17a7-IRES2-Cre;Ai162	321607	F	97, 191
Slc17a7-IRES2-Cre;Ai148	343025	M	77
Slc17a7-IRES2-Cre;Ai148	343027	F	77, 99
Slc17a7-IRES2-Cre;Ai148	329284	M	67
Slc17a7-IRES2-Cre;Ai148	329286	M	67
Slc17a7-IRES2-Cre;Ai148	347103	M	57, 79
Slc17a7-IRES2-Cre;Ai148	347105	F	71
Slc17a7-IRES2-Cre;Ai148	347893	M	67, 75
Slc17a7-IRES2-Cre;Camk2a-tTa;Ai93	303474	F	69, 118
Slc17a7-IRES2-Cre;Camk2a-tTa;Ai93	302981	M	60, 68, 111
Slc17a7-IRES2-Cre;Camk2a-tTa;Ai93	301333	F	67, 118
Slc17a7-IRES2-Cre;Camk2a-tTa;Ai93	306069	F	67, 96
Slc17a7-IRES2-Cre;Camk2a-tTa;Ai93	301329	M	67, 118